https://doi.org/10.5194/egusphere-2026-5064
Preprint. Discussion started: 8 September 2026

The accuracy of barotropic and baroclinic tides in global non-assimilative ocean general circulation models

Joseph K. Ansong[1,2], Brian K. Arbic[2], Romain Bourdalle-Badié[3], Clément Bricaud[3], Jérôme Chanut[3], Dimitris Menemenlis[4], Richard D. Ray[5], Michael Schindelegger[6], Alan J. Wallcraft[7], He Wang[2,8,9], Alistair J. Adcroft[10], Frédéric Briol[11], Maarten C. Buijsman[12], Loren Carrère[11], Eric P. Chassignet[7], Gerald Dibarboure[13], Robert W. Hallberg[8], Christopher N. Hill[14], Ariane Koch-Larrouy[15], Florent Lyard[15], Matthew R. Mazloff[16], An T. Nguyen[17], Nicolas Picot[13], Rui M. Ponte[18], and Jay F. Shriver[19]

[1]Department of Mathematics, University of Ghana, Legon, Accra, Ghana.
[2]Department of Earth & Environmental Sciences, University of Michigan, Ann Arbor, Michigan, USA.
[3]Mercator Ocean International, Toulouse, France
[4]Moss Landing Marine Laboratories, San José State University, San José, California, USA
[5]NASA Goddard Space Flight Center, Greenbelt, Maryland, USA
[6]Institute of Geodesy and Geoinformation, University of Bonn, Bonn, Germany
[7]Center for Oceanic-Atmospheric Prediction Studies, Florida State University, Tallahassee, Florida, USA
[8]Geophysical Fluid Dynamics Laboratory/NOAA, Princeton, NJ, USA
[9]University Corporation for Atmospheric Research, Boulder, CO, USA
[10]Atmospheric and Oceanic Sciences, Princeton University, Princeton, NJ, USA
[11]Space Oceanography Division, Collecte Localisation Satellites, Toulouse, France
[12]School of Ocean Science and Engineering, University of Southern Mississippi, Hattiesburg, Mississippi, USA
[13]Centre National d'Etudes Spatiales, Toulouse, France
[14]Department of Earth, Atmospheric, and Planetary Sciences, Massachusetts Institute of Technology, Cambridge, Massachusetts, USA
[15]CECI CNRS/Cerfacs/IRD, Université de Toulouse, Toulouse, France
[16]Scripps Institution of Oceanography, University of California San Diego, La Jolla, California, USA
[17]Oden Institute for Computational Engineering and Sciences, The University of Texas at Austin, Austin, Texas, USA
[18]Atmospheric and Environmental Research, Lexington, Massachusetts, USA
[19]Oceanography Division, Naval Research Laboratory, Stennis Space Center, Mississippi, USA

Correspondence: Joseph K. Ansong (jkansong@ug.edu.gh)

Abstract. We investigate the accuracy of barotropic tides and phase-locked baroclinic (internal) tides in forward (non-data-assimilative) simulations of four different high-resolution global ocean models: the HYbrid Coordinate Ocean Model (HYCOM), the Modular Ocean Model Version 6 (MOM6), the Nucleus for European Modelling of the Ocean (NEMO), and the Massachusetts Institute of Technology general circulation model (MITgcm). Consistent with a previous study that employed only HYCOM, we find that the phase-locked internal tides in our HYCOM, MOM6 and MITgcm simulations are large relative to altimeter observations unless an explicit parameterized topographic internal wave drag, which damps barotropic and baroclinic tides, is included. We also find that harmonic analysis of long records of model output results in estimates of phase-locked internal tides that compare more favorably with observed baroclinic surface elevations from along-track satellite-altimetry. Increasing the resolution within the same dynamical core reduces amplitudes of phase-locked internal tides, possibly due to a

https://doi.org/10.5194/egusphere-2026-5064
Preprint. Discussion started: 8 September 2026

more efficient energy cascade to higher-frequency internal wave continuum motions. We also document details of the astronomical tidal forcing in the MITgcm runs, which have been widely used by the wideswath altimetry community, that adversely affect the accuracy of modeled barotropic and baroclinic tides. We verify the impacts of the erroneous tidal forcing with results of less expensive shallow-water simulations that also employ the erroneous forcing.

1 Introduction

The flow of barotropic tides over topographic features in the stratified ocean interior results in the generation of internal gravity waves (IGWs) with tidal frequency, known as internal or baroclinic tides. Internal tides may break in the vicinity of topographic features if they have high vertical modes, which are more susceptible to breaking because of their smaller vertical scales. Low-mode internal tides tend to propagate for thousands of kilometers to locations where they dissipate their energy. As internal waves propagate through the ocean, they experience large spatial and temporal variabilities in their energy flux (e.g., Zhao et al. (2010); Rainville et al. (2010); Zaron and Egbert (2014); Ansong et al. (2017)[and references therein]) and dissipate their energy through different mechanisms (e.g., MacKinnon et al. (2017); Ansong et al. (2018)). It is important to study internal tides and higher-frequency IGWs for several reasons, including the fact that, after breaking, they cause diapycnal (or vertical) mixing with subsequent effect on the general ocean circulation (Munk and Wunsch, 1998; Wunsch and Ferrari, 2004).

In concert with observations, global ocean model simulations play a key role in shaping our understanding of the global dynamics of internal tides (Buijsman et al., 2026), and help map the geographical distribution of internal tide hotspots. Modeling internal tides is also important in order to take full advantage of altimetry measurements such as the Surface Water and Ocean Topography (SWOT) altimetry mission (Fu et al., 2024). As stated by several authors (e.g., Arbic et al. (2018); Arbic (2022); Rocha et al. (2016a); Torres et al. (2018)), modeling of global internal tides is critical for the studies that target large-scale non-tidal phenomena and require the accurate removal from altimetry of all nuisance signals, including those associated with tides. In contrast to the one-dimensional measurements of sea surface height (SSH) with conventional nadir satellite altimeters (Fu and Cazenave, 2001), SWOT altimetry provides global SSH measurements in two-dimensional swaths. SWOT is also measuring SSH at smaller horizontal scales. Hence, removing smaller-scale internal tides from SWOT data is of paramount importance for achieving SWOT goals of characterizing the ocean mesoscale and sub-mesoscale circulation.

Internal tides were first directly simulated on basin- and global-scales in three-dimensional ocean models that were forced by only the astronomical tidal potential (Niwa and Hibiya, 2011; Arbic et al., 2004; Simmons et al., 2004). These studies revealed the rich structure of the internal tide geography in the global ocean. Subsequent studies successfully simulated global internal tides by forcing the models with both the astronomical tidal potential and atmospheric fields (Arbic et al., 2010, 2012, 2018; Arbic, 2022; Müller et al., 2012; Waterhouse et al., 2014; Rocha et al., 2016a, b; Qiu et al., 2018; Torres et al., 2018; Buijsman et al., 2020; Fu et al., 2021; Yadidya et al., 2024, 2026).

Although global ocean models appear prominently in the study of internal tides and IGWs, they have several shortcomings. One of these is the inability to resolve breaking IGWs, thereby compelling global ocean models to rely on either explicit parameterizations of internal wave processes, or implicit numerical damping, to capture the effects of energy dissipation due

https://doi.org/10.5194/egusphere-2026-5064
Preprint. Discussion started: 8 September 2026

to breaking high mode waves (e.g., MacKinnon et al. (2017)). A number of studies have emphasized the need for explicit damping mechanisms, such as a parameterized topographic wave drag or some other drag, to obtain accurate tides in forward (non-data-assimilative) global barotropic tide models (e.g., Jayne and St Laurent (2001); Arbic et al. (2004); Egbert et al. (2004); Green and Nycander (2013); Buijsman et al. (2015)). Previous studies utilizing three-dimensional global internal tide models have also shown the importance of having an explicit damping, such as a parameterized wave drag acting on the bottom flow, to account for the generation and breaking of high modes that are unresolved in global models (e.g., Arbic et al. (2004, 2010); Shriver et al. (2012); Ansong et al. (2015); Buijsman et al. (2016, 2020)). As argued in these papers, wave drag is employed as a parameterization of high mode internal tides that break and that are not resolved by discrete global models. Shriver et al. (2012) showed that phase-locked internal tides, as simulated with the application of a parameterized wave drag on the bottom flow, compare reasonably well to satellite altimeter observations. In a subsequent study, Ansong et al. (2015) tested five representative low-mode internal tide damping mechanisms in a high-resolution global ocean model, and compared the results to altimetry-constrained models and observations. The investigation revealed that, without a parameterized topographic wave drag acting on the bottom flow, the phase-locked baroclinic tides become too energetic and propagate too far from their generation sources when compared to satellite observations. In addition, the barotropic tides were found to compare less favorably with the data-assimilative TPXO-atlas (Egbert and Erofeeva, 2002) without a damping mechanism on the barotropic tide. In a related study, Buijsman et al. (2016) found that about 50% of the internal tide dissipation in the simulations examined in that paper is lost to wave drag damping.

This paper focuses on the phase-locked internal tide, which can be written in terms of an amplitude multiplied by a cosine term with a defined phase lag. It is sometimes referred to as the “coherent” or “stationary” internal tide in the literature. Throughout the work, we employ standard harmonic analysis, which by definition picks out the phase-locked component of internal tides, and ignores the non-phase-locked component, sometimes called the “incoherent” or “non-stationary” component.

Here we build upon the work by Ansong et al. (2015), which explored the baroclinic tides in several simulations of the HYbrid Coordinate Ocean Model (HYCOM; Bleck (2002); Chassignet et al. (2003); Halliwell (2004)) and found that a lack of wave drag led to internal tides that are too large relative to altimeter observations. In this paper, we perform a similar investigation using forward (non-data-assimilative) high-resolution simulations of four different global ocean models, all forced simultaneously by atmospheric fields and tides. We employ forward models in this study because more modeling centers are using forward models at this point in time. In addition to HYCOM, the tested models include two simulations of the Massachusetts Institute of Technology general circulation model (MITgcm; Marshall et al. (1997b, a)), two simulations of the Nucleus for European Modelling of the Ocean (NEMO; Madec, G. and NEMO Team (2014)), and two simulations of the Modular Ocean Model Version 6 (MOM6; Adcroft et al. (2019)). These additional models have different numerical implementations compared to the HYCOM simulations and are run by different groups. At present, only HYCOM and MOM6 employ a parameterized topographic wave drag. None of the other simulations employ topographic wave drag or other explicit damping of internal tides. Here we will see whether the barotropic and baroclinic tides in these other simulations are also too large, as are the HYCOM simulations without wave drag, compared to satellite altimeter observations.

https://doi.org/10.5194/egusphere-2026-5064
Preprint. Discussion started: 8 September 2026

We acknowledge that, even without extra explicit damping and even when different models are run at the same horizontal resolution, the internal tide strengths may differ, due to the effects of different numerical damping schemes, different vertical coordinate representations (e.g., z-coordinates vs. isopycnal coordinates vs. terrain-following coordinates), and different vertical resolutions. We therefore suggest that internal tides present an interesting test case for the intercomparison of high-resolution global ocean models. This paper complements the work of Carrère et al. (2021), who performed an intercomparison of several empirical internal tide models, using a forward simulation of one hydrodynamical model (HYCOM) as a reference point. For simplicity, this paper focuses only on M_2, the largest tidal constituent, which by itself is responsible for about 2/3 of the total barotropic tidal kinetic energy, barotropic tidal potential energy, and tidal dissipation across all constituents (Egbert and Ray, 2003).

Because these state-of-the-art global models are often used for operational purposes, such as planning and interpreting SWOT measurements, it is important to compare the simulated internal tides with observations. Ansong et al. (2015) also found that the globally averaged root-mean-square amplitude ($RMSA$) of modeled baroclinic tides compares better to altimetry when long (multi-year) model time series are used in the analysis (see also Colosi and Munk (2006)). Note that this is not a statement about model spin-up; the duration matters even for analyses performed on spun-up model output. The duration of observed time series also matters—see, for instance, Nash et al. (2012)—but our altimeter time series is 17 years long, sufficient to provide robust results. To determine whether the dependence of the RMSA statistics on the length of model records is particular to HYCOM, we also investigate the impact of output duration for the other simulations examined in this paper.

The MITgcm simulation integrated with $1/48°$ horizontal grid spacing, dubbed llc4320, is the highest-resolution simulation assessed in our study. Due to its higher resolution, the llc4320 simulation has a more developed internal gravity wave continuum than other simulations (Savage et al., 2017; Luecke et al., 2020) and forms the basis of more than 200 scientific publications (e.g., Rocha et al. (2016a, b); Savage et al. (2017); Qiu et al. (2018); Torres et al. (2018)). The llc4320 simulation allows us to examine whether the stronger cascade to the internal gravity wave continuum acts as a damping on internal tide motions. In addition, this paper documents some details of the astronomical tidal forcing in the “historic” MITgcm llc4320 run that adversely affect the accuracy of the simulated tides. Using a less computationally expensive hydrodynamic barotropic tide simulation (Schindelegger et al., 2018), we can estimate the tidal errors resulting from the incorrect forcing. Note that llc4320 is currently being re-run with more accurate tidal forcing and other improvements. Tidal accuracy in the new simulations will be examined in separate publications; here we document the tidal accuracy in the widely used historical llc4320 simulations.

There are many factors that will affect analyses of internal tides in the models and altimetry data. The model runs are so computationally expensive that they are rather short, typically of order one year. The nadir altimeter analysis used here, on the other hand, covers 17 years of observations. Internal tides are inherently dependent on the background stratification, which will not be the same in the models as in the actual ocean, especially because the temporal coverage differs from one simulation to another. Furthermore, the stratification varies seasonally and interannually, and the models will not capture that aspect of oceanic variability perfectly either. In addition, the record duration of one of the runs examined here is only six months, meaning that the annual cycle is not fully sampled. Finally, the nadir altimeter data is sampled every 10 days, whereas the output of these model simulations is hourly. The comparisons presented in this study are therefore performed using the datasets

https://doi.org/10.5194/egusphere-2026-5064
Preprint. Discussion started: 8 September 2026

as available, without attempting to reconcile these differences. We acknowledge that some of the differences that we see will be due to the factors above, preventing a fully consistent comparison across all sources.

In Section 2 we describe the different global model simulations employed in this study, and detail the astronomical tidal forcing used in the MITgcm simulations. Section 3 discusses the results of the barotropic and baroclinic analyses, before a summary is given in Section 4.

2 The model simulations and observations

2.1 The HYCOM simulations

The HYCOM outputs used in this paper are the same as those employed in Ansong et al. (2015). The simulations are run in forward (non-data-assimilative) mode on a global tripole grid with a nominal horizontal resolution of $1/12.5°$ and with 41 hybrid vertical layers. The HYCOM simulations employed here do not use data assimilation acting on mesoscale motions; these are not HYCOM forecasts. Thus the HYCOM simulations do not achieve the level of phase accuracy in the internal tides that can be seen in forecasts (Yadidya et al., 2024, 2026). The simulations employed here are forced by the M_2 equilibrium tide and by hourly atmospheric fields from the Navy Global Environmental Model (NAVGEM; Hogan et al. (2014)). The spinup periods for these simulations are described in Ansong et al. (2015). HYCOM has several options for computing the Self Attraction and Loading term (SAL; Hendershott (1972); Ray (1998)), which accounts for the deformation of the solid Earth by the loading of ocean tides, and for the self-gravitation of the so-deformed solid Earth as well as of the ocean tides themselves. In all HYCOM simulations employed in this paper, we use SAL terms calculated offline from the data-assimilative TPXO8-atlas (Egbert and Erofeeva, 2002). The simulations used the topographic wave drag scheme of Jayne and St Laurent (2001). In this scheme, the drag applied depends on the local topographic roughness, the local value of the stratification near the ocean bottom, and the flow strength.

Several internal tide damping mechanisms were considered in Ansong et al. (2015) (see their Table 1). However, only three of the previous wave drag scenarios are revisited here. In experiment “E053”, the topographic wave drag in the model is removed. Experiment “E051” utilizes a topographic wave drag, with a drag scale factor of 0.5. Experiment “E056” is similar to “E051” but with a wave drag scale factor of 0.7. As in Ansong et al. (2015), we also employ an older HYCOM simulation that employs the Garner (2005) drag scheme, and that was run out for a longer period of 5 years (and referred to internally as experiment 18.5; “Expt-18.5”). Experiment E053 is directly comparable to simulations done with other model codes, such as MITgcm and NEMO, that also do not employ an explicit damping on the internal tides. Experiments E051 and E056 inform on the importance of wave drag, as does Experiment 18.5, while the latter also informs about the importance of the duration of the model record.

https://doi.org/10.5194/egusphere-2026-5064
Preprint. Discussion started: 8 September 2026

2.2 The MITgcm simulations

We employ two simulations of MITgcm with horizontal resolutions of $1/12°$ ($3-9$ km grid spacing; referred to as MITgcm12 here and as llc1080 by others), and $1/48°$ ($0.75-2.3$ km grid spacing; referred to as MITgcm48 here and as llc4320 by others) with 90 vertical levels in both simulations. The layer thicknesses range from 1.0 m at the surface to 480 m near the bottom at a maximum model depth of 7 km.

Surface forcing of the MITgcm simulations is done with six-hourly atmospheric fields from the $0.14°$ European Center for Medium-Range Weather Forecasts (ECMWF) atmospheric operational model analysis. Starting in 2011, ECMWF is converted to surface fluxes using the bulk formulae of Large and Yeager (2004). The sea ice model of Losch et al. (2010) is used to compute ocean surface fluxes over ice-covered regions. The MITgcm simulations include atmospheric wind, pressure, and buoyancy forcing, as well as tidal forcing. The MITgcm12 simulation is initialized on January 1, 2010 from a data constrained $1/6°$ simulation provided by the "Estimating the Circulation and Climate of the Ocean, Phase II (ECCO2)" project (Menemenlis et al., 2008). Smaller time steps and Crank-Nicolson barotropic time stepping were used for improved accuracy of barotropic tides representation and energy conservation (Campin et al., 2004). This study employs 6 months of hourly SSH output from MITgcm12, starting from January 1, 2012 to June 30, 2012 and 12 months of hourly SSH output of MITgcm48 from November 13, 2011 to November 12, 2012.

One year of hourly SSH output of the MITgcm48 run is very large (on the order of 8 TB). In response to the large output sizes, we performed an efficient tidal harmonic analysis of the $1/48°$ MITgcm output. We used a novel, computationally optimized, tidal harmonic analysis technique, based on standard least-squares methods (Ponchaut et al., 2001; Pugh and Woodworth, 2014). Specifically, the a priori analysis spectrum includes the most important astronomical constituents in the Darwin development and a few of the more important non-linear waves. The optimization consists of processing the 3D cube, representing the spatio-temporal series to be processed, using the Pangeo software (Eynard-Bontemps et al., 2019) on the CNES HPC. The 3D cube is stored in Zarr format (https://github.com/zarr-developers/zarr-python) in order to optimize concurrent access during the calculation. All the harmonic analyses are scheduled as a calculation graph generated and handled by the Dask library (Dask Development Team, 2016). This solution can process the entire time series in 2.5 hours of computation over 672 processors and 2.5 TB of RAM. The software used for the calculation is available at the following address: https://github.com/CNES/pangeo-pytide.

As described in Arbic et al. (2018), the MITgcm astronomical tidal forcing consists of a full luni-solar tidal potential, applied as an additional atmospheric pressure forcing. Here, for the first time, we document some additional details of two known sources of error in the astronomical tidal forcing in the historic MITgcm llc1080 and llc4320 runs that affect the phases and amplitudes, and thus impact the accuracies of the tides modeled in those runs. The full lunisolar tidal potential was generated using a modified version of the STORMTIDE model of Müller (2013). Later comparisons with other tidal forcing products, after the MITgcm simulations were completed, indicated possible phase errors of several degrees over many tidal frequencies. These phase errors were likely introduced into STORMTIDE by the user at the time of forcing generation and cannot be traced or reproduced. Such biases can partly contribute to the differences in M_2 tidal phases found in the present analysis of the

https://doi.org/10.5194/egusphere-2026-5064
Preprint. Discussion started: 8 September 2026

MITgcm simulations. The second known error is relevant to the SAL term and impacts the magnitude of the applied forcing as follows. The intent in the MITgcm runs was to solve for the pressure gradient relative to the equilibrium tide (astronomical tidal forcing) and the SAL term. Using notation more common to shallow-water models, we write the momentum equation that was intended to be solved, viz.

$$\frac{d\boldsymbol{u}}{dt} + f\hat{k} \times \boldsymbol{u} = -g\nabla(\eta - \eta_{EQ} - \eta_{SAL}) + OT, \tag{1}$$

where $d\boldsymbol{u}/dt$ is the material derivative, $\boldsymbol{u}$ is the horizontal velocity vector, f is the Coriolis parameter, $\hat{k}$ is a unit vector in the local vertical direction, OT denotes "other terms" (including eddy viscosities and wind forcing) in the momentum equation, g is gravitational acceleration, η is the perturbation sea surface height, η_{EQ} is the equilibrium tide, and η_{SAL} is the SAL term (Hendershott, 1972). The intent was to replace the full η_{SAL} term, which is computed more properly using spherical harmonic expansions or integrated Green's functions (Hendershott, 1972; Ray, 1998) with a computationally cheap "scalar approximation", in this case $\eta_{SAL} \approx 0.1121 \cdot \eta$. This scalar approximation was popular some years ago (e.g., Accad and Pekeris (1978)), though in general it is inaccurate and should be abandoned in most modern computations (Ray, 1998). Owing to some miscommunications amongst the implementers, what was actually solved in the MITgcm llc1080 and llc4320 runs was

$$\frac{d\boldsymbol{u}}{dt} + f\hat{k} \times \boldsymbol{u} = -g\nabla(\eta - 1.1121\eta_{EQ}) + OT. \tag{2}$$

In other words, the astronomical tidal forcing was inadvertently too large by a factor of 1.1121, and the SAL term was inadvertently omitted. As noted in several papers dating back to Hendershott (1972), the SAL term strongly impacts the tides in barotropic models. In Section 3.1, we estimate the impact of these unintentional mistakes through implementation of the incorrect tidal forcing given in Equation (2) in the shallow-water barotropic tide model of Schindelegger et al. (2018). We note that an adjustment factor $1 + k_2 - h_2$, where h_2 is the Love number accounting for solid earth deformation and k_2 is the Love number accounting for the perturbations to the gravitational potential resulting from this deformation (Hendershott, 1972), was applied uniformly to η_{EQ} across all frequencies in the MITgcm simulations. Thus, the MITgcm simulations did account for body tides, as did the simulations of other models used in this paper. However, the MITgcm simulations did not account for the small frequency-dependent differences in $1 + k_2 - h_2$ arising from the free core-nutation in the diurnal band (Wahr and Sasao, 1981), which mostly affects our K_1 constituent. We note that astronomical tidal forcing fields were applied to the MITgcm simulations as atmospheric pressure loading from hourly forcing fields linearly interpolated in time.

2.3 The NEMO simulations

The NEMO simulations used in this paper employ the quasi-isotropic ORCA grid (Madec and Imbard, 1996), with equatorial resolutions of $1/12°$ and $1/36°$, and 75 geopotential levels. Vertical resolution ranges from 1 m in the surface layers to 200 m near 5000 m depth.

The NEMO code version used here is v4.2 (Gurvan et al., 2022). NEMO is coupled to a multi-category sea-ice model (Rousset et al., 2015). To allow an accurate representation of the topography, the very last bottom wet cell is adjusted to match

https://doi.org/10.5194/egusphere-2026-5064
Preprint. Discussion started: 8 September 2026

the input bathymetry (Barnier et al., 2006). Ice shelf cavities are explicitly resolved using the parametrization developed by Mathiot et al. (2017). Tidal forcing is applied in NEMO as an additional barotropic force in the momentum equation (see Gurvan et al. (2022)), with a luni-solar astronomical forcing (M_2, S_2, N_2, K_1, O_1), which is refreshed at each sub-iteration of the split-explicit free surface solver. The SAL forcing term for this simulation is taken from the FES2014 data-assimilative tidal model (Lyard et al., 2021). This approach has been preferred to the alternative scalar approximation because it yields more accurate tidal elevations.

This NEMO simulations are driven by 1-hourly and 9-km horizontal resolution atmospheric fields (including surface pressure forcing) issued from ECMWF IFS real-time system. These experiments are initialized from climatological temperature and salinity in October 2012 and run for 3 years until October 2015 without tides. Astronomical tidal forcing is then activated for 3 more years until December 2018, providing sufficient time for tidal internal waves to populate the domain. Results shown are computed over year 2015-2018 from hourly averaged sea-level outputs. The tidal energy budget has been computed from 3 month offline harmonic analysis of three-dimensional (3D) pressure and velocities. The semidiurnal band in that case is defined as a lumped sum of all semidiurnal constituents.

2.4 The MOM6 simulation

Following recommendations of two different workshops (Arbic et al., 2016, 2017), MOM6 is being developed as a near-real-time high-resolution global ocean forecasting system for use by the National Oceanic and Atmospheric Administration (NOAA)(Adcroft et al., 2019; Mouallem et al., 2025). This application of MOM6 is inspired by the Navy use of HYCOM in a similar near-real-time forecasting system. HYCOM was the first widely available ocean model to use the Arbitrary Lagrangian Eulerian (ALE) vertical coordinate system. MOM6 is the most recent model to implement ALE in the vertical direction, and one of its vertical coordinate options is explicitly “HYCOM-like”. MOM6 directly calculates SAL inline using spherical harmonics transformations (Wang et al., 2024), and the wave drag scheme of Jayne and St Laurent (2001) is utilized with a scale factor of 0.7 (which yields the smallest surface tidal error compared with TPXO). MOM6 does directly support floating ice shelves, which is an improvement over HYCOM’s approach of sinking them, but the domain used here does not include a representation of the Antarctic floating ice shelves that have a significant effect on tidal accuracy. The MOM6 simulation with M_2 tides is an extension of twin HYCOM and MOM6 simulations without tides using a configuration similar to the standard 1/12.5° global 41-layer HYCOM setup.

The MOM6 simulation is forced using JRA55 atmospheric reanalysis (Kobayashi et al., 2015). The model is initialized in 1979 and run for 20 years as a spin-up period. M_2 tidal forcing and SAL are introduced on January 1, 1999. The simulation with tidal forcing is then continued for an additional two years, and only the second year is used for the analysis. MOM6 and HYCOM produce very similar tides in this configuration, but the results are less accurate than the standard HYCOM 1/12.5° cases. Some of the potential reasons for the slightly reduced accuracy of tides in the MOM6 simulations relative to the HYCOM simulations include: a) observed SAL from accurate data-constrained barotropic tide models such as TPXO is not used, b) the global domain does not include a representation of the floating Antarctic ice shelves, and c) MOM6 does not employ the Augmented State Ensemble Kalman Filter (ASEnKF) employed in HYCOM (Ngodock et al., 2016).

https://doi.org/10.5194/egusphere-2026-5064
Preprint. Discussion started: 8 September 2026

2.5 Summary of models

Table 1 summarizes the principal numerical characteristics of the simulations employed in this study and highlights several important differences among the four ocean modeling systems. Although all of the simulations solve the primitive equations on global domains and include astronomical tidal forcing alongside atmospheric forcing, they differ substantially in their vertical coordinate systems, horizontal resolution, numerical algorithms, vertical and horizontal eddy viscosity and diffusivity values, and implementation of astronomical tidal forcing and SAL. The table also points out whether the simulations included ice cavities in the Antarctic, a requirement for highly accurate modeling of tides (Genco et al., 1994). These differences provide an opportunity to assess how alternative model formulations influence the simulation of barotropic and baroclinic tides.

One of the most fundamental distinctions among the models is the choice of vertical coordinate. HYCOM and MOM6 both employ Arbitrary Lagrangian-Eulerian (ALE) hybrid coordinates, which allow the model layers to behave as isopycnal coordinates in the stratified open ocean, terrain-following coordinates over shallow shelves, and fixed-depth (z) coordinates in the ocean surface mixed layer and in other weakly stratified parts of the ocean. This flexibility enables improved representation of water-mass structure while avoiding some of the numerical difficulties associated with purely terrain-following or geopotential-coordinate models. In contrast, both NEMO and MITgcm employ geopotential (z-coordinate) discretizations, with NEMO using z^* coordinates that permit a more accurate treatment of the free surface. The vertical resolutions also differ considerably, ranging from 41 layers in HYCOM and MOM6 to 75 levels in NEMO and 90 levels in MITgcm. Because internal tides involve vertical displacements of density surfaces, the choice of vertical coordinate and the vertical resolution both influence the representation of wave propagation, mode structure, and dissipation.

The simulations span a wide range of horizontal resolutions. MOM6 and HYCOM both employ nominal $1/12.5°$ grids, while NEMO includes both $1/12°$ and eddy-rich $1/36°$ configurations, and MITgcm includes both $1/12°$ and the exceptionally high-resolution $1/48°$ (llc4320) configuration. The finest MITgcm grid is approximately four times finer than the standard $1/12°$ simulations and is capable of resolving substantially smaller mesoscale and internal-wave features. As discussed later in the paper, increasing horizontal resolution tends to reduce the strength of the modeled phase-locked internal tide, likely because finer grids permit a more efficient cascade of energy into the unresolved internal-wave continuum and smaller-scale motions. Note that finer-resolution (1/25°) global simulations of HYCOM do exist, but are not employed here.

The analysis periods summarized in Table 1 differ among the simulations. Most simulations provide approximately one year of hourly output, although the MITgcm12 analysis is limited to six months, whereas the MOM6 analysis is based on model years six and seven after an extended spin-up. The differing record lengths should be kept in mind when comparing harmonic analyses, since longer time series generally produce more robust estimates of the phase-locked tidal signal. As demonstrated later in this paper, the duration of the analyzed record can significantly influence the apparent amplitude of the modeled internal tides.

The numerical treatment of momentum diffusion varies considerably between models. Both HYCOM and MOM6 combine Smagorinsky-type viscosity, and MITgcm instead employs the Leith viscosity formulation, whereas NEMO relies primarily on the numerical properties of its discretization and therefore applies no explicit horizontal viscosity. The explicit vertical

https://doi.org/10.5194/egusphere-2026-5064
Preprint. Discussion started: 8 September 2026

viscosities and diffusivities likewise differ by several orders of magnitude among the models, reflecting different turbulence closure strategies and assumptions regarding unresolved vertical mixing processes.

Differences are evident in the tracer diffusion schemes and mixed-layer parameterizations. HYCOM, and MITgcm employ the widely used K-Profile Parameterization (KPP; Large et al. (1994)) for vertical boundary-layer mixing, MOM6 uses the energetics-based planetary boundary layer (ePBL) scheme (Reichl and Hallberg, 2018), whereas NEMO uses a Generic Length Scale (GLS) turbulence closure with a k-epsilon formulation. Only NEMO applies a Gent–McWilliams (GM) isopycnal transport parameterization.

The models differ as well in their numerical advection and time-integration algorithms. MOM6 employs the Piecewise Parabolic Method (PPM), a third-order advection scheme, while HYCOM uses a second-order Flux Corrected Transport (FCT) method. NEMO uses a third-order Upstream Biased Scheme (UBS), and MITgcm employs a seventh-order monotonicity-preserving flux-limited advection algorithm. Likewise, the barotropic and baroclinic time-stepping strategies differ across models, including leapfrog schemes with Asselin filtering, split-explicit approaches, Runge–Kutta integration, and Crank–Nicolson discretization for the external mode. Although these algorithmic differences are primarily motivated by numerical stability and computational efficiency, they also introduce differing amounts of numerical dissipation, which can influence tidal energetics.

Several characteristics listed near the bottom of Table 1 are particularly relevant to tidal modeling. The bottom drag coefficients differ modestly among the models, reflecting different choices for bottom friction. The treatment of Self-Attraction and Loading (SAL), however, varies substantially. MOM6 is the only simulation in this paper that employs an inline SAL (Barton et al., 2022; Brus et al., 2023; Wang et al., 2024), a computation that is dynamically consistent and allows for the SAL effect to act on non-tidal motions, as it does in the actual ocean (Hendershott, 1972). HYCOM employs SAL fields derived from the TPXO data-assimilative tidal atlas, and NEMO uses SAL from the FES2014 tidal model. In contrast, the historical MITgcm simulations considered here do not include a proper SAL correction, an issue that is examined later in this paper. Another important distinction concerns explicit parameterized topographic wave drag. Among the simulations considered here, only HYCOM and MOM6 include the parameterized wave drag of Jayne and St Laurent (2001), which represents the unresolved generation and breaking of high-mode internal tides over rough topography. As demonstrated in subsequent sections, this parameterization plays a critical role in limiting the amplitudes of the simulated phase-locked internal tides.

Finally, Table 1 illustrates that the simulations differ not only in their horizontal and vertical resolutions but also in many aspects of their numerical formulation and physical parameterizations. Consequently, differences in simulated barotropic and baroclinic tides cannot be attributed solely to model resolution. Instead, the results presented in this paper should be interpreted as reflecting the combined effects of vertical coordinate choice, numerical algorithms, turbulence closures, tidal forcing, SAL treatment, parameterized wave drag, and other aspects of model formulation. This diversity makes the present collection of simulations particularly valuable for identifying those model characteristics that exert the strongest influence on the accuracy of simulated barotropic and internal tides.

https://doi.org/10.5194/egusphere-2026-5064
Preprint. Discussion started: 8 September 2026

Table 1. Vertical coordinate, nominal model horizontal grid spacing, integration periods, eddy viscosities and diffusivities, and other characteristics of the simulations used in this study.

Characteristic	MOM6	HYCOM	NEMO12 and NEMO36	MITgcm12 and MITgcm48
Vertical coordinate	41 hybrid ALE layers	41 hybrid ALE layers	75 z*-levels	90 z-levels
Nominal horizontal grid spacing	1/12.5°	1/12.5°	1/12°; 1/36°	1/12°; 1/48°
Analysis period	Model years 6 and 7	1/1/2012– 31/10/2012	01/01/2016– 31/12/2018	1/1/2012– 30/6/2012 and 13/11/2011– 12/11/2012
Explicit horizontal viscosity	Smagorinsky (0.05), Laplacian (A2=0.00286 $\times$ dx m^2 s^{-1}), Biharmonic (A4=-0.02 $\times$ dx^3 m^4 s^{-1})	Smagorinsky (0.05), Laplacian (A2=20 m^2 s^{-1}), Biharmonic (A4=-0.02 $\times$ dx^3 m^4 s^{-1})	None	Leith+
Explicit vertical viscosity (m^2 s^{-1})	3.00e-05	3.00e-05	1.40e-07	5.66e-04
Explicit horizontal diffusivity (m^2 s^{-1})	35	0.005$\times$ dx	0.5*0.018$\times$ dx	0
Explicit vertical diffusivity (m^2 s^{-1})	1.00e-05	1.00e-05	1.40e-7	5.44e-07
Isopycnal scheme (i.e., GM)	None	None	Laplacian	None
Mixed-layer scheme	ePBL	KPP	k-epsilon (GLS) + No penetrative convective algorithm	KPP
Advection scheme	PPM (Huyhn 3rd order)	2nd order FCT	UBS (3rd order)	flux-limited, 7th-order, monotonicity-preserving
Time-stepping scheme	split-explicit, barotropic is 80% forward-backward and 20% backward Euler, baroclinic is RK2	split-explicit, both barotropic and baroclinic use leapfrog with Asselin filter (0.0625)	time splitting. barotropic with LeapFrog+Asselin filter at 0.05	Crank-Nicolson barotropic time stepping
Quadratic bottom drag coefficient	0.003	0.0025	1/12°: 0.0025 ; 1/36° :0.01	0.0021
Surface-current relative wind stress?	yes	yes	no	yes
Ice cavities included?	no	yes	yes	no
SAL used	Inline spherical harmonic SAL	read-in TPXO	read-in FES	none
Tidal forcing	M_2 only	M_2 only	luni-solar, additional barotropic force in the momentum equation	full lunisolar

2.6 Global observational data & diagnostics

The accuracy of the M_2 barotropic tides in all simulations is assessed by comparison against the TPXO8-atlas sea surface elevations (Egbert and Erofeeva, 2002). Other benchmark barotropic tide models, such as FES2014 (Lyard et al., 2021), could just as easily have been used. However, as shown in Stammer et al. (2014), the differences between TPXO and other high-quality barotropic tide models are quite small in the open-ocean, the focus in this paper.

The M_2 baroclinic tides in the models are compared against harmonic constants deduced from 17 years (1992–2008) of along-track TOPEX/Poseidon and Jason satellite altimeter data (Ray and Mitchum, 1996; Shriver et al., 2012). The altimeter harmonic constants apply to the ocean tide alone, as prior models were used to remove signals from all solid tides (both body and load). A prior model of non-tidal ocean variability was also employed, based on multi-mission altimetry (Pascual et al., 2006), which has been found useful for reducing noise in altimeter tide estimates, especially in the vicinity of boundary currents

https://doi.org/10.5194/egusphere-2026-5064
Preprint. Discussion started: 8 September 2026

(Ray and Byrne, 2010). This "mesoscale correction" is capable of introducing new errors from any leakage of tide-model errors in the correction fields (Zaron and Ray, 2018), but in the present application the correction is deemed beneficial.

For the internal tide analysis, the gridded and harmonically analyzed SSH output from all simulations is first interpolated to the altimeter tracks. After this, for both simulations and altimeter output, spatial band-pass filtering along the altimeter tracks is used to extract the internal tide signals with wavelengths in the 50–400-km range. Only locations with sea floor depth greater than 1500 m are examined. In waters with sea floor depth exceeding this threshold, the barotropic tides will have wavelengths much greater than 400 km, such that the filter described above effectively separates barotropic from baroclinic tides. Our figures of barotropic tides only go to $80°$ latitude, and our figures of baroclinic tides only to $60°$ latitude, due to the fact that satellite altimetry does not cover latitudes poleward of $66°$. Other details of the internal tide analysis method can be found in Shriver et al. (2012). As in Ansong et al. (2015), for all models and altimeter observations used here, we compute the globally averaged $RMSA$ of the baroclinic tide SSH. This diagnostic emphasizes the "phase-locked" SSH internal tide signal.

3 Results

3.1 Barotropic Tides

Global maps of the amplitude and phase of M_2 SSH in TPXO and the seven simulations are shown in Fig. 1. The MOM6 simulation without wave drag is denoted as "MOM6-noDrag" and that with wave drag applied is denoted as "MOM6-Drag". In the HYCOM simulation (E051) shown in Fig. 1, wave drag was used. All maps were created from 12 months of SSH output apart from the map made with MITgcm12 (Fig. 1e) which was constructed from 6 months of SSH time series. The surface elevations in the simulations include the baroclinic tide but are dominated by the barotropic tide. Qualitatively, we see that the spatial distribution of the barotropic tide amplitude in HYCOM, NEMO and MOM6-Drag (Figs. 1b-1d, 1h) compare reasonably well with those of TPXO, although MOM6 exhibits unrealistically large barotropic amplitudes in the Weddell Sea. HYCOM, NEMO and MOM6-Drag also correctly capture almost all amphidromic locations except at the Antarctic coast around $160°$ W where NEMO, MITgcm and MOM6 deviate somewhat from TPXO. NEMO shows reasonably accurate tides without the use of a damping mechanism; we will discuss this in more detail below. Unlike HYCOM and NEMO, MITgcm and MOM6-noDrag generally exhibit comparatively large barotropic amplitudes (Fig. 1e-1g). MOM6-noDrag has exceptionally large amplitudes in the Atlantic Ocean, in particular around the coast of Brazil and the North-East Atlantic (Figure 1g), while MITgcm exhibits amplitudes that are too large in the Pacific Ocean, especially around the Tasman Sea and close to the Solomon Islands (Fig. 1e-1f). Substantial barotropic phase errors are also seen in both simulations of MITgcm. Table 2 quantifies some of the discrepancies between the simulations and TPXO. For instance, the globally averaged $RMSA$ of the barotropic tide (in deep water with depths $>$ 1000 m and equatorward of latitude $66°$), in HYCOM and NEMO, compare well to TPXO.

The comparatively large barotropic amplitudes in MOM6-noDrag and MITgcm are most likely due to the absence of an explicit damping mechanism in these simulations. In addition, as described in Section 2.2, the MITgcm tides are large in part due to inadvertent mistakes in astronomical tidal forcing. We reiterate that, in Fig. 1, only the HYCOM (experiment E051) and MOM6-Drag simulations employ a wave drag scheme. The other simulations do not have any explicit damping mechanism.

https://doi.org/10.5194/egusphere-2026-5064
Preprint. Discussion started: 8 September 2026

Without a wave drag, HYCOM equally exhibits barotropic tides that are too large compared to TPXO (e.g., Ansong et al. (2015); their Figs. 2e-2f) just as we find in MOM6-noDrag. NEMO behaves somewhat differently, in that it exhibits accurate barotropic tides without the need for an additional explicit parameterized topographic internal wave drag.

Table 2. The second row displays the globally averaged $RMSA$ of the barotropic tide in deep water (depths $>$ 1000 m) and equatorward of latitude 66°, compared to the TPXO value (in brackets). The variations in the TPXO value with each model are due to the fact that the TPXO data is first interpolated to each model grid before computing the $RMSA$. The third row is the globally averaged $RMSA$ of the baroclinic tide (equatorward of latitude 63.5° and in deep water, depths $>$ 1500 m), adjusted for record duration, and application of the correction factor for MITgcm runs. The along-track altimeter $RMSA$ value is 0.46 cm. The last row shows the ratio of baroclinic to barotropic globally averaged RMSA.

	NEMO12 (no drag)	HYCOM12 (drag)	MOM6 (no drag)	MOM6 (drag)	MITgcm12 (no drag)	MITgcm48 (no drag)
$RMSA\ (cm)$ Barotropic	28.2 (25.9)	28.9 (28.4)	31.8 (26.5)	26.6 (26.5)	35.6 (26.5)	34.3 (26.5)
$RMSA\ (cm)$ Baroclinic	0.47	0.48	0.56	0.51	0.66	0.59
Ratio	0.017	0.017	0.018	0.019	0.019	0.017

We employ a barotropic tide model to estimate the magnitude of the errors in the MITgcm simulation due to the mistakes, described earlier, in the astronomical tidal forcing of that simulation. The barotropic tidal amplitude of the shallow water barotropic tide model of Schindelegger et al. (2018), based on codes by Einšpigel and Martinec (2017) and run at $1/8^\circ$ horizontal resolution, is displayed in Fig. 2. The M_2 barotropic tidal amplitudes in the control simulation in Figure 2a mimic the M_2 barotropic tidal amplitudes in TPXO (see Fig. 1a). In a second simulation with the barotropic model (Figure 2b; designated as “No SAL”), the SAL term was removed and the amplitude of the equilibrium tide increased by a factor of 1.1121. Figure 2b shows that this second simulation roughly captures the spatial distribution of the amplitude of the barotropic tide in the MITgcm simulations (see Figs. 1e-1f; compare especially the area around New Zealand and on the equator north of New Zealand). Some of the incorrect tidal features in the MITgcm simulations therefore are due to the omission of the SAL. We compute the barotropic kinetic energy (KE) in the control run and the no-SAL runs to be 1.82 and 2.51 ($\times 10^{17}$ J) respectively. The available potential energy (APE) is 1.58 and 2.03 ($\times 10^{17}$ J) respectively. Thus, the impacts of the inadvertent mistakes in the MITgcm astronomical tidal forcing can be estimated by computing the ratio of the barotropic tidal kinetic energy in the no-SAL run in Fig. 2 to that in the control run. This ratio is 1.38, meaning that the incorrect astronomical tidal forcing will by itself artificially enhance amplitudes of the internal tides, which are created by barotropic tidal flows, in the MITgcm runs by the square root of this number, in other words, 1.17. The equivalent number for the barotropic tidal available potential energy

https://doi.org/10.5194/egusphere-2026-5064
Preprint. Discussion started: 8 September 2026

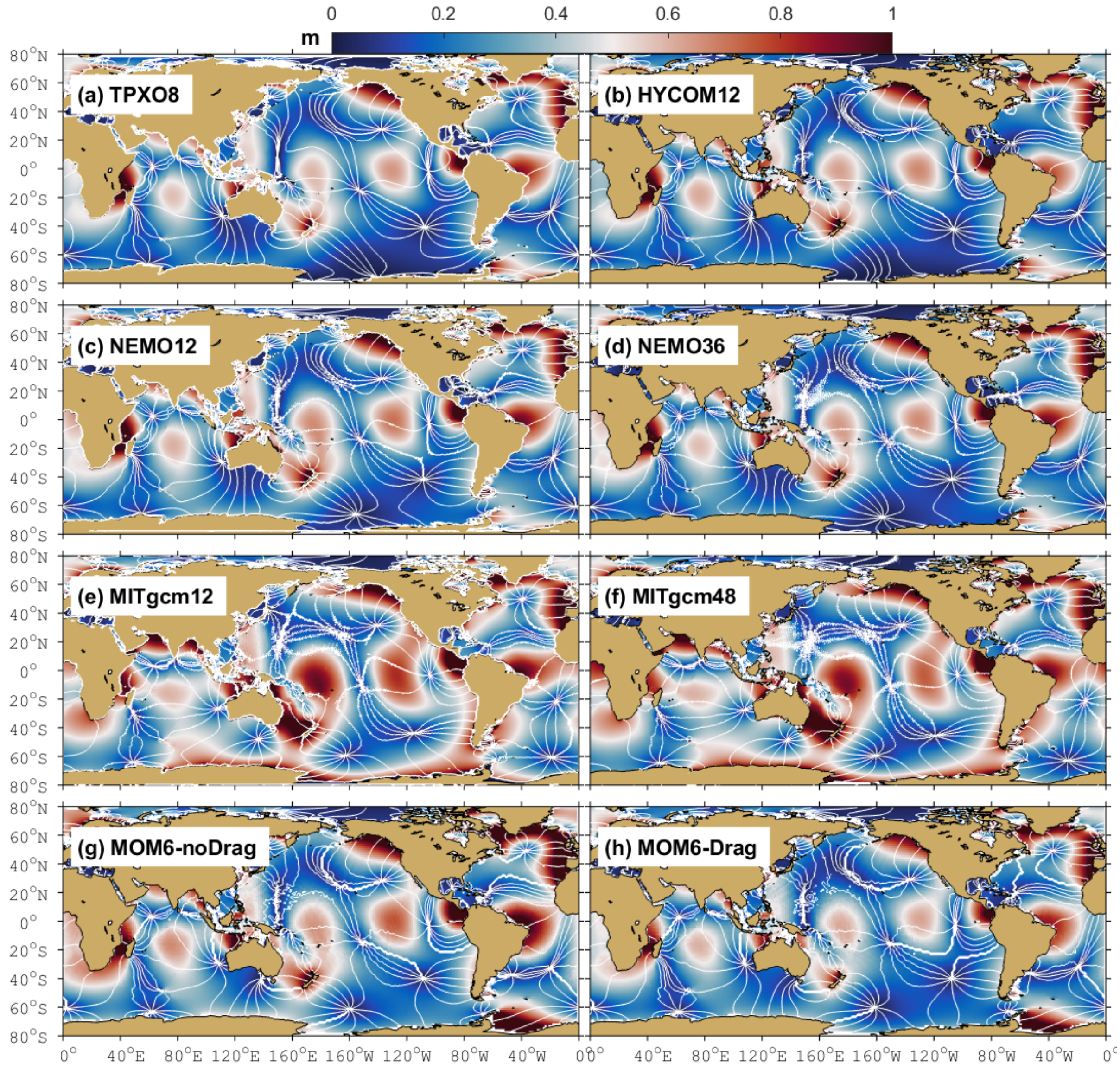

Figure 1. Amplitude (colors) and phase (white contours separated by 30°) of the M_2 surface elevation in (a) TPXO8-atlas, a barotropic tide model constrained by satellite altimetry, and simulations from (b) HYCOM (experiment “E051" with a topographic wave drag scale factor of 0.5), (c) NEMO12, (d) NEMO36, (e) MITgcm12, (f) MITgcm48, (g) MOM6-noDrag, and (h) MOM6-Drag. The M_2 SSH amplitudes in the simulations include both barotropic and baroclinic components. With the exception of the HYCOM and MOM6-Drag simulations, all other numerical simulations shown in this figure are run without a parameterized topographic wave drag.

https://doi.org/10.5194/egusphere-2026-5064
Preprint. Discussion started: 8 September 2026

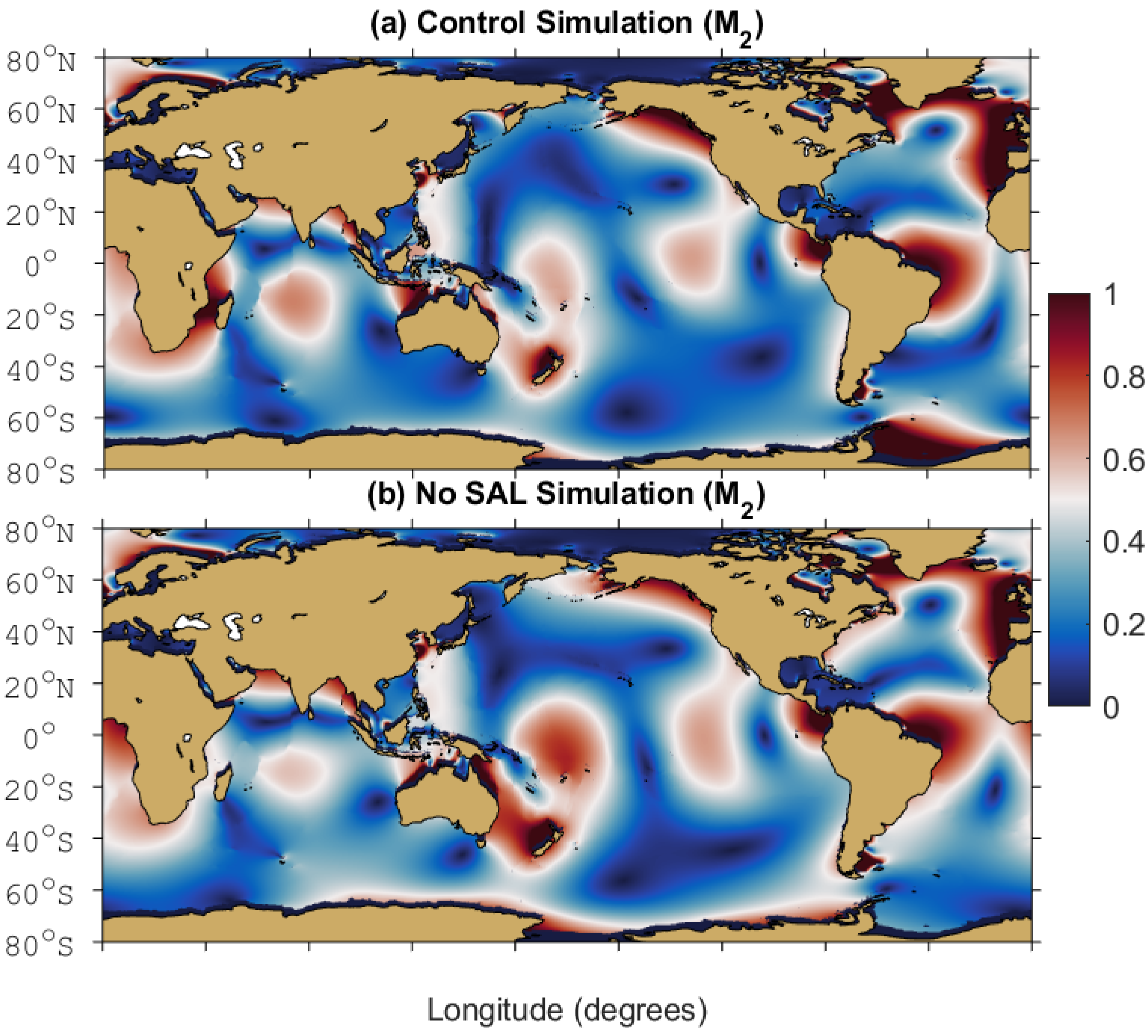

Figure 2. (a) Amplitudes of the M_2 surface elevations, from the shallow-water barotropic tide model of Schindelegger et al. (2018). (b) Same as in (a) but without the SAL term in the momentum equation, and with an astronomical tidal forcing that is increased by a factor of 1.1121, in order to mimic the forcing of the MITgcm simulations shown here.

is 1.28, meaning that barotropic tidal elevations in the MITgcm runs will be artificially enhanced by the square root of this number, 1.13, due to the incorrect tidal forcing.

3.2 Baroclinic Tides

The globally averaged $RMSA$ of the baroclinic tide from all simulations, as a function of the length of model time series, is given in Fig. 3, together with the $RMSA$ from along-track altimetry (0.46 cm). The plots in Fig. 3a contain results from the

https://doi.org/10.5194/egusphere-2026-5064
Preprint. Discussion started: 8 September 2026

HYCOM simulations used in Ansong et al. (2015) for comparison to the other global simulations discussed here. Figure 3a also contains simulations from MOM6, showing that MOM6-Drag performs better than MOM6-noDrag for all lengths of model time series used in the analysis. Nevertheless, HYCOM simulations ("E056") run with the same wave drag scale factor (0.7) as MOM6-Drag, perform slightly better than the MOM6-Drag in the long run. Using an older HYCOM experiment ("Expt-18.5"), that was run for a longer time, Ansong et al. (2015) found that the baroclinic amplitudes converge to an asymptotic value after about 4 years (see also Buijsman et al. (2020)). Figure 3b demonstrates that the $RMSA$ in the other global ocean simulations also depends on record duration. All the results shown in Fig. 3b are from simulations without any wave drag mechanism in the model. As in Ansong et al. (2015), we use the Expt-18.5 results as a correction to the $RMSA$ values, and the asymptotic values are displayed at month 60 in Fig. 3. It is interesting that without applying wave drag, MOM6 shows better RMSA results than HYCOM (Fig. 3b), but HYCOM performs better than MOM6 when using wave drag (Fig. 3a).

Figure 3c displays the $RMSA$ for MITgcm simulations with and without applying the correction factor deduced in Section 3.1. The MITgcm $RMSA$, especially for MITgcm48, gets closer to the observed value upon dividing the amplitude by the correction factor of 1.17. As stated in Ansong et al. (2015) for HYCOM simulations, we find here that both the record duration and the topographic wave drag have significant impact on the stationary internal tide amplitudes. The quantification of tidal record duration as a function of geographical location in HYCOM was investigated in Buijsman et al. (2020). The dependence of internal tide amplitude estimates on record duration depends on the details of sea level spectra in the tidal bands, particularly the magnitudes and shapes of tidal cusps, and on the inherent spectral resolution of each time series (Colosi and Munk, 2006).

Figure 4 displays global maps of baroclinic tidal amplitudes from the along-track altimeter data and the simulations, wherein the HYCOM simulations are experiments E051 (with wave drag; HYCOM12-Drag) and E053 (without wave drag; HYCOM12-noDrag). The maps have been corrected for the effect of record duration and, in addition, the MITgcm correction factor was applied to the MITgcm maps. Based upon our experience in Ansong et al. (2015), we expected internal tides in simulations with some kind of damping mechanism to lie closer to observations than internal tides in simulations without such damping. Indeed, the HYCOM12-Drag and MOM6-Drag maps (Figs. 4b, 4h) exhibit closer resemblance to the altimeter amplitudes (Fig. 4a) than do the HYCOM-noDrag, MOM6-noDrag and MITgcm internal tide maps. However, the NEMO simulations lie close to altimetry values despite the lack of internal wave drag in NEMO. With the notable exception of the NEMO simulations, compared to the along-track altimeter amplitudes, the baroclinic tides in simulations without wave drag are too large and propagate too far from the hotspots (Figs. 4c, 4f-g, 4i), consistent with the findings in Ansong et al. (2015) for HYCOM simulations without a topographic wave drag. Relative to altimetry, MITgcm12 exhibits the largest globally averaged baroclinic amplitudes (see Table 2). The lower amplitudes of internal tides in MITgcm48 compared to MITgcm12 may be due to the fact that MITgcm48 has a more fully developed internal gravity wave continuum spectrum (e.g., Rocha et al. (2016a); Savage et al. (2017); Luecke et al. (2020)), and the development of this spectrum drains energy from the internal tide. Indeed, Skitka et al. (2024) showed that the profile of internal gravity wave dissipation in high-resolution regional MITgcm simulations compares well with observations, supporting the idea that MITgcm48 figures realistic amounts of internal wave dissipation.

The larger internal tides in runs without wave drag are due in part to the lack of damping on the internal tides themselves, and in part due to the fact that barotropic tides are larger in runs without wave drag. To crudely isolate these two effects, we provide

https://doi.org/10.5194/egusphere-2026-5064
Preprint. Discussion started: 8 September 2026

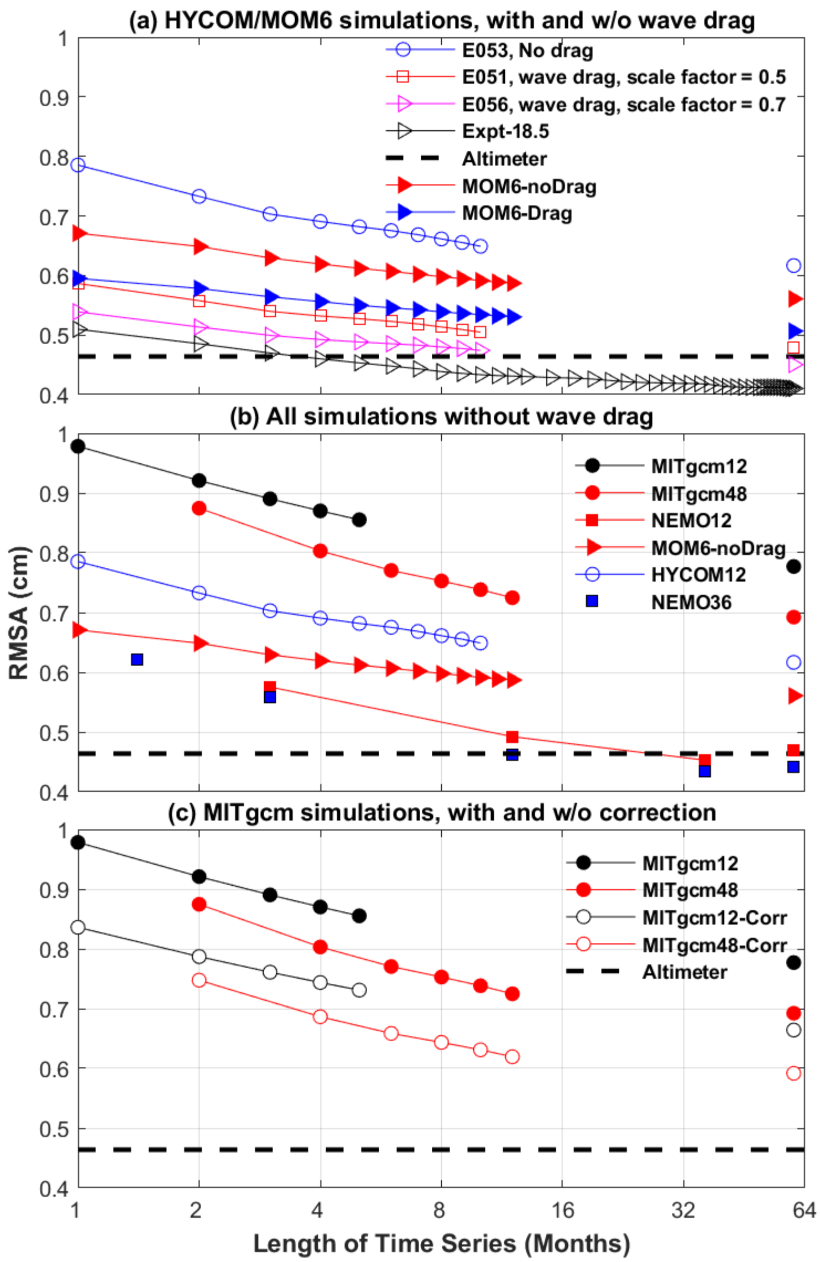

Figure 3. Globally-averaged root-mean-square amplitude, $RMSA$, of simulated baroclinic tidal elevations versus length of simulation time series used in the analysis. The x-axis is a base 2 log scale. Values computed from global altimetry data are also given. (a) HYCOM12 and MOM6 results with and without wave drag. Expt-18.5 is an older HYCOM experiment about which several papers have been written (e.g., Shriver et al. (2012)) and from which 5-year-long SSH output was stored. (b) Results from all simulations that do not employ a parameterized topographic wave drag. (c) MITgcm simulations with and without a correction factor for erroneous tidal forcing as described in Section 3.1. The amplitudes shown at month 60 are estimates based on changes of internal tide amplitude with record length in HYCOM Expt-18.5.

https://doi.org/10.5194/egusphere-2026-5064
Preprint. Discussion started: 8 September 2026

in Table 2 the ratio of the globally averaged $RMSA$ values of the internal and barotropic tides, for all of the simulations examined here. The ratio varies from 1.70% to 1.92%, a relatively constant range that indeed indicates correlation between the amplitudes of baroclinic and barotropic tides.

4 Summary and Conclusions

This paper builds upon the previous work of Carrère et al. (2021), who analyzed the internal tides in several models derived from empirical analysis of satellite nadir altimetry (and also included one non-assimilative hydrodynamical HYCOM simulation). The current study also builds upon Ansong et al. (2015), who investigated the effects of damping mechanisms on the internal tides in HYCOM. The Ansong et al. (2015) study revealed that without an explicit drag scheme acting on the tidal flow, the internal tides become too energetic and propagate too far from their sources. Ansong et al. (2015) also discovered that, apart from employed dampings, the record duration used in the analysis of the internal tides also plays a key role in comparison of modeled internal tides to those derived from satellite observations. However, one of the shortcomings of the Ansong et al. (2015) paper was the use of only one global model (HYCOM) in their analysis.

To address this shortcoming, the present paper investigates the internal tides and the importance of damping in global high-resolution simulations of four different global ocean general circulation models. All of the simulations used here were run at a nominal resolution of $1/12°$, except for MITgcm48 and NEMO36 which are run at nominal resolutions of $1/48°$ and $1/36°$ respectively. Consistent with the Ansong et al. (2015) results, we find here that the absence of a drag scheme in MITgcm and MOM6-noDrag results in overly energetic internal tides (Fig. 4f-g, 4i). The baroclinic tides are too energetic in part because the barotropic tides, which generate the internal tides, are too energetic in HYCOM, MITgcm, and MOM6 runs that do not contain wave drag. The internal tides in NEMO compare reasonably well to along-track altimetry, although the simulations in NEMO were run without a wave drag. This may be because the NEMO simulations employ high vertical resolution, which potentially enhances (i) the energy cascade from low-mode internal tides to higher-vertical mode motions and (ii) the dissipation of those vertical modes in the model. Differences in numerical schemes almost certainly have an effect as well. Conversely, it appears that the MOM6 and MITgcm simulations, and to a lesser extent the HYCOM simulations, require the insertion of an explicit parameterization of damping, which is generally done with a parameterized wave drag here, in order to obtain accurate barotropic tides. It is important to note that in some models, internal tides may be damped more strongly than, for instance, lower-frequency motions such as mesoscale eddies. Internal tides thus present themselves as an interesting test of the impact of vertical resolution, numerics, and other characteristics of high-resolution model simulations. Further work on the strengths of mesoscale eddies and internal tides in models versus observations is needed to more fully flesh out these points. As in Ansong et al. (2015) and Buijsman et al. (2020), we also find that record duration strongly affects the comparison of modeled internal tides to observations.

In the course of this study, we discovered some unintentional mistakes that were made in the implementation of the astronomical tidal forcing in the particular MITgcm llc4320 simulations, which have been used in many studies beginning with Rocha et al. (2016a, b). The astronomical tidal forcing was inadvertently too large by a factor of 1.1121, and the SAL term

https://doi.org/10.5194/egusphere-2026-5064
Preprint. Discussion started: 8 September 2026

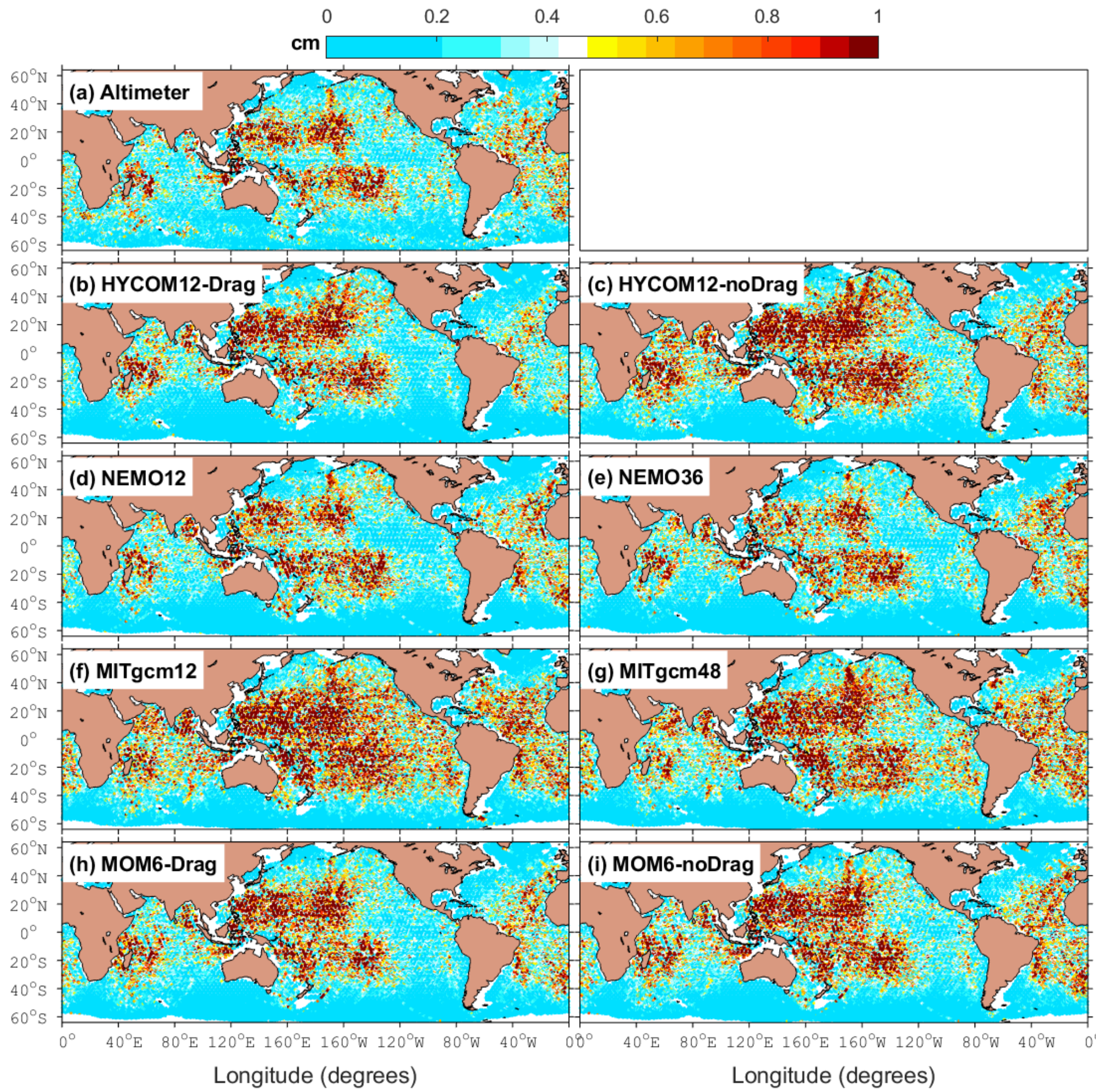

Figure 4. Amplitude (cm) of M_2 internal tides in (a) along-track altimeter-based analyses, and in (b) HYCOM (Experiment E051, with wave drag), (c) HYCOM (Experiment E053, no wave drag), (d) NEMO12, (e) NEMO36, (f) MITgcm12, (g) MITgcm48, (h) MOM6-Drag, (i) MOM6-noDrag. The amplitudes of the MITgcm12 simulation are computed from 6 months of SSH output, while all others are based on 12 months of output.

https://doi.org/10.5194/egusphere-2026-5064
Preprint. Discussion started: 8 September 2026

was omitted. Here we estimate the impacts of these mistakes in the MITgcm tidal forcing by implementing the incorrect tidal forcing in the shallow-water barotropic tide model of Schindelegger et al. (2018), and computing the ratio of the barotropic tidal kinetic energy in this run to that in a control run with correct astronomical tidal forcing. The result yields estimates of the artificial enhancements to the barotropic and baroclinic tides in the MITgcm simulations due to the errors in the astronomical tidal forcing (see sections 2.2 and 3.1). The astronomical tidal forcing errors have been corrected in newer high-resolution MITgcm simulations that are currently in production.

We have focused on internal tide sea surface height amplitudes here, but models can be compared with other datasets. For instance, Luecke et al. (2020) compared low- and high-frequency kinetic energies and temperature variance in HYCOM and MITgcm llc4320 with observations from historical moored instruments. Yu et al. (2019) compared low- and high-frequency surface kinetic energies in MITgcm48 and surface drifters. Yu et al. (2019) found that MITgcm48 semidiurnal surface KE is larger than that in the drifters by a factor of about 4, a larger discrepancy than we find here for surface elevations. Because wave drag acts on flows, it may affect kinetic energy more than elevations of internal tides. Arbic et al. (2022) showed that the HYCOM surface semidiurnal KE is much closer to the drifters than MITgcm48 is.

We have focused here on parameterized topographic wave drag as a means of damping low-mode internal tides in models. This is a deliberate choice, as topographic wave drag is a damping mechanism present in HYCOM that can be tuned. Such drag is a stand-in for the fact that the generation and breaking of high mode internal tides is not resolved in global internal wave models. There are other mechanisms for internal tide damping in the ocean, such as wave-wave interactions in the upper ocean, breaking on shelves, interactions with the mean flow and eddies, amongst others (e.g., McComas and Bretherton (1977); Müller et al. (1986); Staquet and Sommeria (2002); Nash et al. (2004); Martini et al. (2011); Kelly et al. (2013); Waterhouse et al. (2014); St. Laurent and Garrett (2002); Rainville and Pinkel (2006); Dunphy and Lamb (2014); Kerry et al. (2014); Ansong et al. (2018)). In future work, we will attempt to parameterize some of the latter damping processes as well as damping processes near ocean bathymetric features. The fact that the internal tides in MITgcm48 are weaker than in MITgcm12 indicates potential promise in damping modeled internal tides through leakage of energy into the internal gravity wave continuum spectrum, which is more fully developed in MITgcm48 than in MITgcm12; the latter paradigm was successfully explored in Skitka et al. (2024).

Data availability.

MITgcm LLC4320 output is available at https://www.poseidon-ocean.net/products/datasets/llc4320-dataset/. Global NEMO output is available at s3.waw3-1.cloudferro.com/ORCA36/HARMONICS/. Model outputs analysed in this study, together with plotting codes used to reproduce the figures, have been archived on Zenodo and are available at https://doi.org/10.5281/zenodo.21642660 (Ansong and Arbic, 2026).

Author contributions.

https://doi.org/10.5194/egusphere-2026-5064
Preprint. Discussion started: 8 September 2026

Conceptualization: Joseph K. Ansong, Brian K. Arbic **Data curation:** Joseph K. Ansong **Funding acquisition:** Brian K. Arbic **Investigation:** Joseph K. Ansong, Brian K. Arbic, Romain Bourdalle-Badié, Clément Bricaud, Jérôme Chanut, Matthew R. Mazloff, Dimitris Menemenlis, An T. Nguyen, Rui M. Ponte, Richard D. Ray, Michael Schindelegger, Alan J. Wallcraft, He Wang **Methodology:** Joseph K. Ansong, Brian K. Arbic, Romain Bourdalle-Badié, Clément Bricaud, Frédéric Briol, Loren Carrère, Jérôme Chanut, Eric P. Chassignet, Gerald Dibarboure, Matthew R. Mazloff, Dimitris Menemenlis, An T. Nguyen, Nicolas Picot, Rui M. Ponte, Richard D. Ray, Michael Schindelegger, Alan J. Wallcraft, He Wang **Project Administration:** Joseph K. Ansong, Brian K. Arbic **Resources:** Alistair J. Adcroft, Brian K. Arbic, Romain Bourdalle-Badié, Clément Bricaud, Frédéric Briol, Jérôme Chanut, Eric P. Chassignet, Robert W. Hallberg, Christopher N. Hill, Ariane Koch-Larrouy, Florent Lyard, Dimitris Menemenlis, Nicolas Picot, Richard D. Ray, Michael Schindelegger, Jay F. Shriver, Alan J. Wallcraft, He Wang **Visualization:** Joseph K. Ansong, Brian K. Arbic **Writing – original draft:** Joseph K. Ansong, Brian K. Arbic **Writing – review & editing:** Alistair J. Adcroft, Joseph K. Ansong, Brian K. Arbic, Clément Bricaud, Frédéric Briol, Maarten C. Buijsman, Loren Carrère, Jérôme Chanut, Eric P. Chassignet, Matthew R. Mazloff, Dimitris Menemenlis, Rui M. Ponte, An T. Nguyen, Richard D. Ray, Michael Schindelegger, Alan J. Wallcraft

Competing interests.

The authors declare that they have no conflict of interest.

Acknowledgements. JKA and BKA acknowledge funding from the University of Michigan Associate Professor Support Fund, supported by the Margaret and Herman Sokol Faculty Awards, and from National Science Foundation (NSF) grant OCE-0968783; the latter was part of a multi-institution Climate Process Team grant, led by Professor Jennifer MacKinnon of UCSD. B.K.A., M.C.B., and J.F.S. also acknowledge funding from NASA grants NNX13AD95G, NNX16AH79G, NNX17AH55G, and 80NSSC20K1135. JFS, JGR, and AJW, were supported by the projects "Eddy resolving global ocean prediction including tides" and "Ageostrophic vorticity dynamics" sponsored by the ONR under program element 0602435N, and by N00014-11-1-2288. JFS acknowledges support from the Office of Naval Research (ONR) through grant N0001426GI01612 as part of the Global Internal Waves project under the National Oceanographic Partnership Program (https://nopp.giw.ucsd.edu). MS was supported by the German Research Foundation (DFG, project no. 451039647). This work was supported in part by a grant of computer time from the Department of Defense (DoD) High Performance Computing Modernization Program at the Navy DoD Supercomputing Resource Center. This research was made possible, in part, by the OSiRIS project at University of Michigan and by computing resources provided by the NASA Advanced Supercomputing (NAS) Division of the Ames Research Center. DM carried out research at the Jet Propulsion Laboratory, California Institute of Technology, under contract with NASA, with support from the Physical Oceanography and Modeling, Analysis, and Prediction Programs. This is NRL contribution XXXXXX and has been approved for public release.

https://doi.org/10.5194/egusphere-2026-5064
Preprint. Discussion started: 8 September 2026

References

Accad, Y. and Pekeris, C. L.: Solution of the tidal equations for the M_2 and S_2 tides in the world oceans from knowledge of the tidal potential alone, Philosophical Transactions of the Royal Society, 290, 235–266, 1978.

Adcroft, A., Anderson, W., Balaji, V., Blanton, C., Bushuk, M., Dufour, C. O., Dunne, J. P., Griffies, S. M., Hallberg, R., Harrison, M. J., Held, I. M., Jansen, M. F., John, J. G., Krasting, J. P., Langenhorst, A. R., Legg, S., Liang, Z., McHugh, C., Radhakrishnan, A., Reichl, B. G., Rosati, T., Samuels, B. L., Shao, A., Stouffer, R., Winton, M., Wittenberg, A. T., Xiang, B., Zadeh, N., and Zhang, R.: The GFDL Global Ocean and Sea Ice Model OM4.0: Model Description and Simulation Features, Journal of Advances in Modeling Earth Systems, 11 (10), https://doi.org/10.1029/2019MS001726, 2019.

Ansong, J. K. and Arbic, B. K.: Dataset of the accuracy of barotropic and baroclinic tides in global non-assimilative ocean general circulation models, Zenodo, https://doi.org/10.5281/zenodo.21642660, 2026.

Ansong, J. K., Arbic, B. K., Buijsman, M. C., Richman, J. G., Shriver, J. F., and Wallcraft, A. J.: Indirect evidence for substantial damping of low-mode internal tides in the open ocean, Journal of Geophysical Research Oceans, 120, 6057–6071, https://doi.org/10.1002/2015JC010998, 2015.

Ansong, J. K., Arbic, B. K., Buijsman, M. C., Alford, M. H., Zhao, Z., Harper, L., Timko, P. G., Richman, J. G., Metzger, E. J., Shriver, J. F., and Wallcraft, A. J.: Semidiurnal internal tide energy fluxes and their variability in a global ocean model and moored observations, Journal of Geophysical Research Oceans, 122 (3), 1882–1900, https://doi.org/10.1002/2016JC012184, 2017.

Ansong, J. K., Arbic, B. K., Harper, L., Alford, M. H., Buijsman, M. C., Timko, P. G., Richman, J. G., Shriver, J. F., and Wallcraft, A. J.: Geographical distribution of diurnal and semidiurnal Parametric Subharmonic Instability in a global ocean circulation model, Journal of Physical Oceanography, 48, 1409–1431, https://doi.org/10.1175/JPO-D-17-0164.1, 2018.

Arbic, B. K.: Incorporating tides and internal gravity waves within global ocean general circulation models: A review, Progress in Oceanography, 206, 102 824, https://doi.org/10.1016/j.pocean.2022.102824, 2022.

Arbic, B. K., Garner, S. T., Hallberg, R. W., and Simmons, H. L.: The accuracy of surface elevations in forward global barotropic and baroclinic tide models, Deep-Sea Research II, 51, 3069–3101, 2004.

Arbic, B. K., Wallcraft, A. J., and Metzger, E. J.: Concurrent simulation of the eddying general circulation and tides in a global ocean model, Ocean Modelling, 32, 175–187, 2010.

Arbic, B. K., Richman, J. G., Shriver, J. F., Timko, P. G., Metzger, E. J., and Wallcraft, A. J.: Global modeling of internal tides within an eddying ocean general circulation model, Oceanography, 25 (2), 20–29, 2012.

Arbic, B. K., Hallberg, R. W., Mehra, A., Richman, J. G., (Organizers), and Attendees, O.: Workshop on Improving ALE Ocean Modeling, NOAA Center for Weather and Climate Prediction, College Park, MD, October 3-4, 2016, https://arbic.earth.lsa.umich.edu/wp-content/uploads/2018/03/workshopreport_final.pdf, 2016.

Arbic, B. K., Carman, J., Hallberg, R. W., James, S., McCarren, D., Mehra, A., Richman, J. G., (Organizers), and Attendees, O.: Arbitrary Lagrangian-Eulerian (ALE) Working Group Meeting, NOAA, Silver Spring, MD, May 9-10, 2017, https://arbic.earth.lsa.umich.edu/wp-content/uploads/2018/03/draftsummary_2017vi02clean.docx, 2017.

Arbic, B. K., Alford, M. H., Ansong, J. K., Buijsman, M., Ciotti, R. B., Farrar, J. T., Hallberg, R. W., Henze, C. E., Hill, C. N., Luecke, C. A., Menemenlis, D., Metzger, E. J., Müller, M., Nelson, A. D., Nelson, B. C., Ngodock, H. E., Ponte, R. M., Richman, J. G., Savage, A. C., Scott, R. B., Shriver, J. F., Simmons, H. L., Souopgui, I., Timko, P. G., Wallcraft, A. J., Zamudio, L., and Zhao, Z.: A Primer

https://doi.org/10.5194/egusphere-2026-5064
Preprint. Discussion started: 8 September 2026

on Global Internal Tide and Internal Gravity Wave Continuum Modeling in HYCOM and MITgcm, in: New Frontiers in Operational Oceanography*(eds. Chassignet)*, chap. 13, pp. 307–391, GODAE OceanView, 2018.

Arbic, B. K., Elipot, S., Brasch, J. M., Menemenlis, D., Ponte, A. L., Shriver, J. F., Yu, X., Zaron, E. D., Alford, M. A., Buijsman, M. C., Abernathey, R., Garcia, D., Guan, L., Martin, P. E., and Nelson, A. D.: Near-surface oceanic kinetic energy distributions from drifter observations and numerical models, Journal of Geophysical Research: Oceans, 127, e2022JC018 551, https://doi.org/10.1029/2022JC018551, 2022.

Barnier, B., Madec, G., Penduff, T., Molines, J.-M., Tréguier, A.-M., Le Sommer, J., Beckmann, A., Biastoch, A., Böning, C., Dengg, J., Derval, C., Durand, E., Gulev, S., Remy, E., Talandier, C., Theetten, S., Maltrud, M., McClean, J., and de Cuevas, B.: Impact of partial steps and momentum advection schemes in a global ocean circulation model at eddy-permitting resolution, Ocean Dynamics, 56, 543–567, https://doi.org/10.1007/s10236-006-0082-1, 2006.

Barton, K. N., Pal, N., Petersen, M. R., Arbic, B. K., Engwirda, D., Roberts, A. F., Westerink, J. J., Wirasaet, D., and Schindelegger, M.: Global barotropic tide modeling using inline self-attraction and loading in MPAS-Ocean, Journal of Advances in Modeling Earth Systems, 14, e2022MS003 207, https://doi.org/https://doi.org/10.1029/2022MS003207, 2022.

Bleck, R.: An oceanic general circulation model framed in hybrid isopycnic-Cartesian coordinates, Ocean Modelling, 37, 55–88, 2002.

Brus, S. R., Barton, K. N., Pal, N., Roberts, A. F., Engwirda, D., Petersen, M. R., Arbic, B. K., Wirasaet, D., Westerink, J. J., and Schindelegger, M.: Scalable self attraction and loading calculations for unstructured ocean tide models, Ocean Modelling, 182, 102 160, https://doi.org/https://doi.org/10.1016/j.ocemod.2023.102160, 2023.

Buijsman, M. C., Arbic, B. K., Green, J. A. M., Helber, R. W., Richman, J. G., Shriver, J. F., Timko, P. G., and Wallcraft, A. J.: Optimizing internal wave drag in a forward barotropic model with semidiurnal tides, Ocean Modelling, 85, 42–55, 2015.

Buijsman, M. C., Ansong, J. K., Arbic, B. K., Richman, J. G., Shriver, J. F., Timko, P. G., Wallcraft, A. J., Whalen, C. B., and Zhao, Z.: Impact of internal wave drag on the semidiurnal energy balance in a global ocean circulation model, Journal of Physical Oceanography, 46, 1399–1419, https://doi.org/10.1175/JPO-D-15-0074.1, 2016.

Buijsman, M. C., Stephenson, G. R., Ansong, J. K., Arbic, B. K., Green, J. A. M., Richman, J. G., Shriver, J. F., Vic, C., Wallcraft, A. J., and Zhao, Z.: On the interplay between horizontal resolution and wave drag and their effect on tidal baroclinic mode waves in realistic global ocean simulations, Ocean Modelling, 152, 101 656, https://doi.org/10.1016/j.ocemod.2020.101656, 2020.

Buijsman, M. C., Waterhouse, A. F., Zaron, E. D., Yadidya, B., Xu, C., Whitley, V., Wenegrat, J. O., Wang, J., Wallcraft, A. J., Varma, D., Tchonang, B. C., Siyanbola, O., Shriver, J. F., Sheremet, V. A., Send, U., Raja, K. J., Polzin, K., Ngodock, H. E., Moulin, A. J., Meiners, G., Lucas, A. J., Lankhorst, M., Kuehl, J. J., Kelly, S. M., Kachelein, L., Huang, Y., Griffin, C., Girton, J. B., Farrar, J. T., Delpech, A., Chen, Z., Chassignet, E. P., Carrier, M. J., Bracco, A., Arbic, B. K., Andres, M., and Abdulfatai, M. A.: A Multiagency Experiment on Internal Wave Energy, Mixing, and Interactions and Their Representation in Global Ocean Models and Operational Forecasts, Bulletin of the American Meteorological Society, 107, E158 – E182, https://doi.org/10.1175/BAMS-D-24-0174.1, 2026.

Campin, J.-M., Adcroft, A., Hill, C., and Marshall, J.: Conservation of properties in a free-surface model, Ocean Modelling, 6, 221–244, https://doi.org/10.1016/S1463-5003(03)00009-X, 2004.

Carrère, L., Arbic, B. K., Dushaw, B., Egbert, G., Erofeeva, S., Lyard, F., Ray, R. D., Ubelmann, C., Zaron, E., Zhao, Z., Shriver, J. F., Buijsman, M. C., and Picot, N.: Accuracy assessment of global internal-tide models using satellite altimetry, Ocean Science, 17, 147–180, https://doi.org/10.5194/os-17-147-2021, 2021.

Chassignet, E. P., Smith, L. T., Halliwell, G. R., and Bleck, R.: North Atlantic Simulations with the Hybrid Coordinate Ocean Model (HYCOM): Impact of the Vertical Coordinate Choice, Reference Pressure, and Thermobaricity, Journal of Physical Oceanography, 33, 2504–2526, 2003.

Colosi, J. and Munk, W.: Tales of the venerable Honolulu tide gauge, Journal of Physical Oceanography, 36, 967–996, https://doi.org/10.1175/JPO2876.1, 2006.

Dask Development Team: Dask: Library for dynamic task scheduling, url: https://dask.org, 2016.

Dunphy, M. and Lamb, K. G.: Focusing and vertical mode scattering of the first mode internal tide by mesoscale eddy interaction, Journal of Geophysical Research, 119, 523–536, 2014.

Egbert, G. D. and Erofeeva, S. Y.: Efficient inverse modeling of barotropic ocean tides, Journal of Atmospheric and Oceanic Technology, 19, 183–204, 2002.

Egbert, G. D. and Ray, R. D.: Semi-diurnal and diurnal tidal dissipation from TOPEX/Poseidon altimetry, Geophysical Research Letters, 30 (17), https://doi.org/10.1029/2003GL017676, 2003.

Egbert, G. D., Ray, R. D., and Bills, B. G.: Numerical modeling of the global semidiurnal tide in the present day and in the Last Glacial Maximum, Journal of Geophysical Research, 109, https://doi.org/10.1029/2003JC001973, 2004.

Einšpigel, D. and Martinec, Z.: Time-domain modeling of global ocean tides generated by the full lunisolar potential, Ocean Dynamics, 67, 165–189, https://doi.org/10.1007/s10236-016-1016-1, 2017.

Eynard-Bontemps, G., Abernathey, R., Hamman, J., Ponte, A., and Rath, W.: The Pangeo Big Data Ecosystem and its use at CNES, in: Proceedings of 2019 Big Data from Space (BiDS'19), Publications Office of the European Union, http://publications.jrc.ec.europa.eu/repository/handle/JRC115761, 2019.

Fu, H., Wu, X., Li, W., Zhang, L., Liu, K., and Dan, B.: Improving the accuracy of barotropic and internal tides embedded in a high-resolution global ocean circulation model of MITgcm, Ocean Modelling, 162, 101 809, https://doi.org/10.1016/j.ocemod.2021.101809, 2021.

Fu, L. L. and Cazenave, A.: Satellite Altimetry and Earth Sciences: A Handbook of Techniques and Applications, Academic Press, San Diego, 2001.

Fu, L. L., Pavelsky, T., Cretaux, J. F., Morrow, R., Farrar, J. T., Vaze, P., Sengenes, P., Vinogradova-Shiffer, N., Sylvestre-Baron, A., Picot, N., and Dibarboure, G.: The Surface Water and Ocean Topography Mission: A breakthrough in radar remote sensing of the ocean and land surface water, Geophysical Research Letters, 51, e2023GL107 652, https://doi.org/https://doi.org/10.1029/2023GL107652, 2024.

Garner, S. T.: A topographic drag closure built on an analytical base flux, Journal of Atmospheric Science, 62, 2302–2315, 2005.

Genco, M., Lyard, F., and Le Provost, C.: The oceanic tides in the South Atlantic Ocean, Annales Geophysicae, 12, 868–886, https://doi.org/10.1007/s00585-994-0868-8, 1994.

Green, J. A. M. and Nycander, J.: A Comparison of Tidal Conversion Parameterizations for Tidal Models, Journal of Physical Oceanography, 43, 104–119, 2013.

Gurvan, M., Bourdallé-Badie, R., Chanut, J., Clementi, E., Coward, A., Ethé, C., Iovino, D., Lea, D., Lévy, C., Lovato, T., Martin, N., Masson, S., Mocavero, S., Rousset, C., Storkey, D., Müeller, S., Nurser, G., Bell, M., Samson, G., Mathiot, P., Mele, F., and Moulin, A.: NEMO ocean engine, https://doi.org/10.5281/zenodo.6334656, 2022.

Halliwell, G. R.: Evaluation of vertical coordinate and vertical mixing algorithms in the HYbrid-Coordinate Ocean Model (HYCOM), Ocean Modelling, 7, 285–322, 2004.

Hendershott, M. C.: The effects of solid earth deformation on global ocean tides., Geophysical Journal of the Royal Astronomical Society, 29, 389–402, https://doi.org/10.1111/j.1365-246X.1972.tb06167.x, 1972.

https://doi.org/10.5194/egusphere-2026-5064
Preprint. Discussion started: 8 September 2026

Hogan, T. F., Liu, M., Ridout, J. A., Peng, M. S., Whitcomb, T. R., Ruston, B. C., Reynolds, C. A., Eckermann, S. D., Moskaitis, J. R., Baker, N. L., McCormack, J. P., Viner, K. C., McLay, J. G., Flatau, M. K., Xu, L., Chen, C., and Chang, S. W.: The Navy Global Environmental Model, Oceanography, 27(3), 116–125, http://dx.doi.org/10.5670/oceanog.2014.73, 2014.

Jayne, S. R. and St Laurent, L. C.: Parameterizing tidal dissipation over rough topography, Geophysical Research Letters, 28, 811–814, 2001.

Kelly, S. M., Jones, N. L., Nash, J. D., and Waterhouse, A. F.: The geography of semidiurnal mode-1 internal-tide energy loss, Geophysical Research Letters, 40, 4689–4693, https://doi.org/10.1002/grl.50872, 2013.

Kerry, C., Powell, B., and Carter, G.: The impact of subtidal circulation on internal-tide-induced mixing in the Philippine Sea, Journal of Physical Oceanography, 44, 3209–3224, https://doi.org/10.1175/JPO-D-13-0142.1, 2014.

Kobayashi, S., Ota, Y., Harada, Y., Ebita, A., Moriya, M., Ebina, H., Onoda, S., Onogi, K., Kamahori, H., Kobayashi, C., Endo, H., Takahashi, K., Fukagata, N., and Kawase, K.: The JRA-55 Reanalysis: General Specifications and Basic Characteristics, Journal of the Meteorological Society of Japan. Ser. II, 93, 5–48, https://doi.org/10.2151/jmsj.2015-001, 2015.

Large, W. G. and Yeager, S. G.: Diurnal and decadal global forcing for ocean and sea-ice models: The data sets and climatologies, NCAR Tech. Note, Boulder, CO, https://doi.org/10.5065/D6KK98Q6, tN–460+ST (May), 2004.

Large, W. G., McWilliams, J. C., and Doney, S. C.: Oceanic vertical mixing: a review and a model with a nonlocal boundary layer parameterization, Reviews of Geophysics, 32, 363–403, 1994.

Losch, M., Menemenlis, D., Campin, J.-M., Heimbach, P., and Hill, C. N.: On the formulation of sea-ice models. Part 1: effects of different solver implementations and parameterizations, Ocean Modelling, 33, 129–144, https://doi.org/10.1016/j.ocemod.2009.12.008, 2010.

Luecke, C. A., Arbic, B. K., Richman, J. G., Shriver, J. F., Alford, M. H., Ansong, J. K., L, B. S., Buijsman, M. C., Menemenlis, D., Scott, R. B., Timko, P. G., Voet, G., Wallcraft, A. J., and Zamudio, L.: Statistical comparisons of temperature variance and kinetic energy in global ocean models and observations: Results from mesoscale to internal wave frequencies, Journal of Geophysical Research Oceans, 125, e2019JC015 306, https://doi.org/10.1029/2019JC015306, 2020.

Lyard, F., Allain, D. J., Cancet, M., Carrère, L., and Picot, N.: FES2014 global ocean tide atlas: design and performance, Ocean Science, 17, 615–649, https://doi.org/https://doi.org/10.5194/os-17-615-2021, 2021.

MacKinnon, J. A., Zhao, Z., Whalen, C. B., Waterhouse, A. F., Trossman, D. S., Sun, O. M., St. Laurent, L. C., Simmons, H. L., Polzin, K., Pinkel, R., Pickering, A., Norton, N. I., Nash, J. D., Musgrave, R., Merchant, L. M., Melet, A. V., Mater, B., Legg, S., Large, W. G., Kunze, E., Klymak, J. M., Jochum, M., Jayne, S. R., Hallberg, R. W., Griffies, S. M., Diggs, S., Danabasoglu, G., Chassignet, E. P., Buijsman, M. C., Bryan, O. F., Briegleb, B. P., Barna, A., Arbic, B. K., Ansong, J. K., and Alford, M. H.: Climate Process Team on internal-wave driven ocean mixing, Bulletin of the American Meteorological Society, pp. 2429–2454, https://doi.org/10.1175/BAMS-D-16-0030.1, 2017.

Madec, G. and Imbard, M.: A global ocean mesh to overcome the North Pole singularity, Climate Dynamics, 12, 381–388, https://doi.org/10.1007/bf00211684, 1996.

Madec, G. and NEMO Team: NEMO Reference Manual, Ocean Dynamics Component: NEMO-OPA, Institut Pierre-Simon Laplace (IPSL), France, ISSN No: 1288-1619, 2014.

Marshall, J., Adcroft, A., Hill, C., Perelman, L., and Heisey, C.: A finite-volume, incompressible Navier Stokes model for studies of the ocean on parallel computers, Journal of Geophysical Research Oceans, 102 (C3), 5753–5766, https://doi.org/10.1029/96JC02775, 1997a.

Marshall, J., Hill, C., Perelman, L., and Adcroft, A.: Hydrostatic, quasi-hydrostatic, and nonhydrostatic ocean modeling, Journal of Geophysical Research Oceans, 102 (C3), 5733–5752, https://doi.org/10.1029/96JC02776, 1997b.

https://doi.org/10.5194/egusphere-2026-5064
Preprint. Discussion started: 8 September 2026

Martini, K. I., Alford, M. H., Kunze, E., Kelly, S. M., and Nash, J. D.: Observations of internal tides on the Oregon continental slope, Journal of Physical Oceanography, 41, 1772–1794, 2011.

Mathiot, P., Jenkins, A., Harris, C., and Madec, G.: Explicit representation and parametrised impacts of under ice shelf seas in the z^* coordinate ocean model NEMO 3.6, Geoscientific Model Development, 10, 2849–2874, https://doi.org/10.5194/gmd-10-2849-2017, 2017.

McComas, C. H. and Bretherton, F. P.: Resonant interactions of oceanic internal waves, Journal of Physical Oceanography, 82(9), 1397–1412, 1977.

Menemenlis, D., Campin, J. M., Heimbach, P., Hill, C. N., Lee, T., Nguyen, A. T., Schodlok, M. P., and Zhang, H.: ECCO2: High resolution global ocean and sea ice data synthesis, Mercator Ocean Quarterly Newsletter, pp. 13–21, 2008.

Mouallem, J., Gao, K., Reichl, B., Chilutti, L., Harris, L., Benson, R., Zadeh, N., Chen, J., Chen, J., and Zhang, C.: Development of a High-Resolution Coupled SHiELD-MOM6 Model. Part I–Model Overview, Coupling Technique, and Validation in a Regional Setup, EGUsphere, pp. 1–29, 2025.

Müller, M.: On the space- and time-dependence of barotropic-to-baroclinic tidal energy conversion, Ocean Modelling, 72, 242–252, https://doi.org/10.1016/j.ocemod.2013.09.00, 2013.

Müller, M., Cherniawsky, J. Y., Foreman, M. G. G., and Storch von, J. S.: Global M_2 internal tide and its seasonal variability from high resolution ocean circulation and tide modeling, Geophysical Research Letters, 39, L19607, https://doi.org/10.1029/2012GL053320, 2012.

Müller, P., Holloway, G., Henyey, F., and Pomphrey, N.: Nonlinear interactions among internal gravity waves, Reviews of Geophysics, 24(3), 493–536, 1986.

Munk, W. and Wunsch, C.: Abyssal recipes II: energetics of tidal and wind mixing, Deep-Sea Research I, 45, 1977–2010, 1998.

Nash, J. D., Kunze, E., Toole, J. M., and Schmitt, R. W.: Internal tide reflection and turbulent mixing on the continental slope, Journal of Physical Oceanography, 34, 1117–1134, 2004.

Nash, J. D., Shroyer, E. L., Kelly, S. M., Inall, M. E., Duda, T. F., Levine, M. D., Jones, N. L., and Musgrave, R. C.: Are any coastal internal tides predictable?, Oceanography, 25(2), 80–95, https://doi.org/http://dx.doi.org/10.5670/oceanog.2012.44, 2012.

Ngodock, H. E., Souopgui, I., Wallcraft, A. J., Richman, J. G., Shriver, J. F., and Arbic, B. K.: On improving the accuracy of the M_2 barotropic tides embedded in a high-resolution global ocean circulation model, Ocean Modelling, 97, 16–26, https://doi.org/10.1016/j.ocemod.2015.10.011, 2016.

Niwa, Y. and Hibiya, T.: Estimation of baroclinic tide energy available for deep ocean mixing based on three-dimensional global numerical simulations, Journal of Oceanography, 67, 493–502, 2011.

Pascual, A., Faugère, Y., Larnicol, G., and Le Traon, P.-Y.: Improved description of the ocean mesoscale variability by combining four satellite altimeters, Geophysical Research Letters, 33, L02 611, https://doi.org/10.1029/2005GL024633, 2006.

Ponchaut, F., Lyard, F., and Le Provost, C.: An analysis of the tidal signal in the WOCE Sea Level Dataset, Journal of Atmospheric and Oceanic Technology, 18(1), https://doi.org/10.1175/1520-0426(2001)018<0077:AAOTTS>2.0.CO;2, 2001.

Pugh, D. T. and Woodworth, P. L.: Sea Level Science: Understanding Tides, Surges, Tsunamis and Mean Sea-Level Changes, Cambridge Univ. Press, Cambridge, 2014.

Qiu, B., Chen, S., Klein, P., Wang, J.and Torres, H., Fu, L.-L., and Menemenlis, D.: Seasonality in transition scale from balanced to unbalanced motion in the world ocean, Journal of Physical Oceanography, 48, 591–605, https://doi.org/10.1175/JPO-D-17-0169.1, 2018.

Rainville, L. and Pinkel, R.: Baroclinic Energy Flux at the Hawaiian Ridge: Observations from the R/P FLIP, Journal of Physical Oceanography, 36, 1104–1122, 2006.

Rainville, L., Shaun Johnston, T. M., Carter, G. S., Merrifield, M. A., Pinkel, R., Worcester, P. F., and Dushaw, B. D.: Interference pattern and propagation of the M_2 internal tide south of the Hawaiian Ridge, Journal of Physical Oceanography, 40, 311–325, 2010.

Ray, R. D.: Ocean self-attraction and loading in numerical tidal models, Marine Geodesy, 21, 181–192, https://doi.org/10.1080/01490419809388134, 1998.

Ray, R. D. and Byrne, D. A.: Bottom pressure tides along a line in the southeast Atlantic Ocean and comparisons with satellite altimetry, Ocean Dynamics, 60, 1167–1176, 2010.

Ray, R. D. and Mitchum, G. T.: Surface manifestation of internal tides generated near Hawaii, Geophysical Research Letters, 23, 2101–2104, 1996.

Reichl, B. G. and Hallberg, R.: A simplified energetics based planetary boundary layer (ePBL) approach for ocean climate simulations, Ocean Modelling, 132, 112–129, https://doi.org/10.1016/j.ocemod.2018.10.004, 2018.

Rocha, C. B., Chereskin, T. K., Gille, S. T., and Menemenlis, D.: Mesoscale to submesoscale wavenumber spectra in Drake Passage, Journal of Physical Oceanogarphy, 46, 601–620, https://doi.org/10.1175/JPO-D-15-0087.1, 2016a.

Rocha, C. B., Chereskin, T. K., Gille, S. T., and Menemenlis, D.: Seasonality of submesoscale dynamics in the Kuroshio Extension, Journal of Geophysical Research, 43 (21), 11 304–11 311, https://doi.org/10.1002/2016GL071349, 2016b.

Rousset, C., Vancoppenolle, M., Madec, G., Fichefet, T., Flavoni, S., Barthélemy, A., Benshila, R., Chanut, J., Lévy, C., Masson, S., , and Vivier, F.: The Louvain-La-Neuve sea ice model LIM3.6: global and regional capabilities, Geoscience Model Development, 8, 2991–3005, 2015.

Savage, A. C., Arbic, B. K., Alford, M. H., Ansong, J. K., Farrar, J. T., Menemenlis, D., O'Rourke, A. K., Richman, J. G., Shriver, J. F., Wallcraft, A. J., and Zamudio, L.: Spectral decomposition of internal gravity waves sea surface height in global models, Journal of Geophysical Research: Oceans, 122, https://doi.org/10.1002/2017JC013009, 2017.

Schindelegger, M., Green, J., Wilmes, S.-B., and Haigh, I.: Can we model the effect of observed sea level rise on tides?, Journal of Geophysical Research: Oceans, 123, https://doi.org/10.1029/2018JC013959, 2018.

Shriver, J. F., Arbic, B. K., Richman, J. G., Ray, R. D., Metzger, E. J., Wallcraft, A. J., and Timko, P. G.: An evaluation of the barotropic and internal tides in a high resolution global ocean circulation model, Journal of Geophysical Research, 117, C10024, https://doi.org/10.1029/2012JC008170, 2012.

Simmons, H. L., Hallberg, R. W., and Arbic, B. K.: Internal wave generation in a global baroclinic tide model, Deep-Sea Research II, 51, 3043–3068, 2004.

Skitka, J., Arbic, B. K., Ma, Y., Momeni, K., Pan, Y., Peltier, W. R., Menemenlis, D., and Thakur, R.: Internal-wave dissipation mechanisms and vertical structure in a high-resolution regional ocean model, Geophysical Research Letters, 51, e2023GL108 039, https://doi.org/ttps://doi.org/10.1029/2023GL108039, 2024.

St. Laurent, L. and Garrett, C.: The role of internal tides in mixing the deep ocean, Journal of Physical Oceanography, 32, 2882–2899, 2002.

Stammer, D., Ray, R. D., Andersen, O. B., Arbic, B. K., Bosch, W., Carrère, L., Cheng, Y., Chinn, D. S., Dushaw, B. D., Egbert, G. D., Erofeeva, S. Y., Fok, H. S., Green, J. A. M., Griffiths, S., King, M. A., Lapin, V., Lemoine, F. G., Luthcke, S., Lyard, F., Morison, J., Müller, M., Padman, L., Richman, J. G., Shriver, J. F., Shum, C. K., Taguchi, E., and Yi, Y.: Accuracy assessment of global barotropic ocean tide models, Reviews of Geophysics, 52, https://doi.org/10.1002/2014RG000450, 2014.

Staquet, C. and Sommeria, J.: Internal gravity waves: From instability to turbulence, Annual Review of Fluid Mechanics, 34, 559–593, 2002.

https://doi.org/10.5194/egusphere-2026-5064
Preprint. Discussion started: 8 September 2026

Torres, H. S., Klein, P., Menemenlis, D., Qiu, B., Su, Z., Wang, J., Chen, S., and Fu, L.-L.: Partitioning Ocean Motions Into Balanced Motions and Internal Gravity Waves: A Modeling Study in Anticipation of Future Space Missions, Journal of Geophysical Research: Oceans, 123, 8084–8105, https://doi.org/10.1029/2018JC014438, 2018.

Wahr, J. M. and Sasao, T.: A diurnal resonance in the ocean tide and in the Earth's load response due to the resonant free 'core nutation', Geophysical Journal of the Royal Astronomical Society, 64, 747–765, 1981.

Wang, H., Hallberg, R., Wallcraft, A. J., Arbic, B. K., and Chassignet, E. P.: Improving global barotropic tides with sub-grid scale topography, Journal of Advances in Modeling Earth Systems, 16, e2023MS004 056, https://doi.org/https://doi.org/10.1029/2023MS004056, 2024.

Waterhouse, A. J., MacKinnon, J. A., Nash, J. D., Alford, M. H., Kunze, E., Simmons, H. L., Polzin, K. L., St. Laurent, L. C., Sun, O. M., Pinkel, R., Talley, L. D., Whalen, C. B., Huussen, T. N., Carter, G. S., Fer, I., Waterman, S., Garabato, A. C. N., Sanford, T. B., and Lee, C. M.: Global Patterns of Diapycnal Mixing from Measurements of the Turbulent Dissipation Rate, Journal of Physical Oceanography, 44, 1854–1872, 2014.

Wunsch, C. and Ferrari, R.: Vertical mixing, energy and the general circulation of the ocean., Annual Review of Fluid Mechanics, 36, 281–314, 2004.

Yadidya, B., Arbic, B. K., Shriver, J. F., Nelson, A. D., Zaron, E. D., Buijsman, M. C., and Thakur, R.: Phase-accurate internal tides in a global ocean forecast model: Potential applications for nadir and wide-swath altimetry, Geophysical Research Letters, 51, e2023GL107 232, https://doi.org/10.1029/2023GL107232, 2024.

Yadidya, B., Arbic, B. K., Zaron, E. D., Shriver, J. F., Buijsman, M. C., Chassignet, E. P., Carrère, L., and Tchilibou, M.: A global internal tide modeling framework for improving satellite observations of fine-scale ocean circulation, Science Advances, 12, eaee1885, https://doi.org/10.1126/sciadv.aee1885, 2026.

Yu, X., Ponte, A. L., Elipot, S., Menemenlis, D., Zaron, E. D., and Abernathey, R.: Surface kinetic energy distributions in the global oceans from a high-resolution numerical model and surface drifter observations, Geophysical Research Letters, 46, 9757–9766, https://doi.org/10.1029/2019GL083074, 2019.

Zaron, E. D. and Egbert, G. D.: Time-variable refraction of the internal tide at the Hawaiian Ridge, Journal of Physical Oceanography, 44, 538–557, https://doi.org/10.1175/JPO-D-12-0238.1, 2014.

Zaron, E. D. and Ray, R. D.: Aliased tidal variability in mesoscale sea level anomaly maps, Journal of Atmospheric and Oceanic Technology, 35, 2421–2435, https://doi.org/10.1175/JTECH-D-18-0089.1, 2018.

Zhao, Z., Alford, M. H., MacKinnon, J. A., and Pinkel, R.: Long-range propagation of the semi-diurnal internal tide from the Hawaiian ridge, Journal of Physical Oceanography, 40, 713–736, 2010.